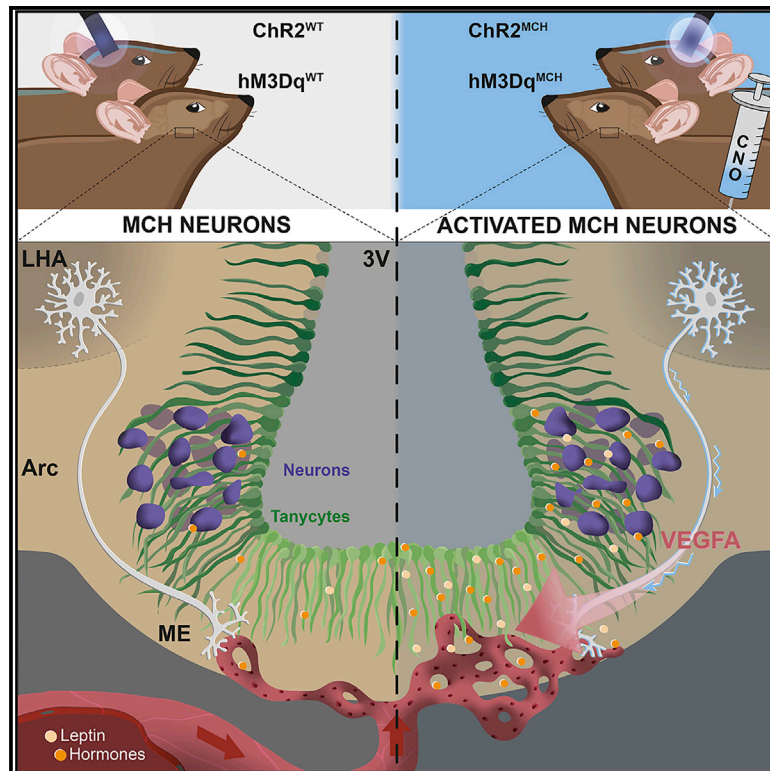# MCH Neurons Regulate Permeability of the Median Eminence Barrier

Graphical Abstract

Authors

Hong Jiang, Sarah Gallet,
Paul Klemm, ..., Markus Schwaninger,
Vincent Prevot, Jens C. Brüning

Correspondence

bruening@sf.mpg.de

In Brief

Melanin-concentrating hormone (MCH)-expressing neurons in the lateral hypothalamus are regulators of energy homeostasis and sleep. Here, Jiang et al. report that they provide dense projection to the median eminence. MCH neuron activation enhances permeability of the median eminence barrier through increasing microvessel fenestration, thus facilitating leptin access to the hypothalamus.

Highlights

- MCH neurons provide dense projections to the median eminence

- MCH neuron activation promotes permeability of the median eminence barrier

- MCH neuron activation enhances microvessel fenestration in the ME

- MCH neuron activation enhances leptin action in the arcuate nucleus

CellPress

Article

MCH Neurons Regulate Permeability of the Median Eminence Barrier

Hong Jiang,[1,2,3] Sarah Gallet,[4] Paul Klemm,[1,2,3] Pia Scholl,[1,2,3] Kat Folz-Donahue,[5] Janine Altmüller,[6] Jens Alber,[1,2,3] Christian Heilinger,[1,2,3] Christian Kukat,[5] Anne Loyens,[4] Helge Müller-Fielitz,[7] Sivaraj Sundaram,[7] Markus Schwaninger,[7] Vincent Prevot,[4] and Jens C. Brüning[1,2,3,8,9,*]

[1]Max Planck Institute for Metabolism Research, Department of Neuronal Control of Metabolism, Gleueler Str. 50, 50931 Cologne, Germany
[2]Center for Endocrinology, Diabetes and Preventive Medicine (CEDP), University Hospital Cologne, Kerpener Str. 26, 50924 Cologne, Germany
[3]Excellence Cluster on Cellular Stress Responses in Aging Associated Diseases (CECAD) and Center of Molecular Medicine Cologne (CMMC), University of Cologne, Joseph-Stelzmann-Str. 26, 50931 Cologne, Germany
[4]University of Lille, Inserm, CHU Lille, Lille Neuroscience & Cognition Research Center, Development and Plasticity of the Neuroendocrine Brain, UMR-S1172, Lille, France
[5]Max Planck Institute for Biology of Ageing, FACS Core Facility, Gleueler Str. 50, 50931 Cologne, Germany
[6]University of Cologne, Cologne Center for Genomics, Cologne, Germany
[7]University of Lübeck, Institute of Experimental and Clinical Pharmacology and Toxicology, Ratzeburger Allee 16023562 Lübeck, Germany
[8]National Center for Diabetes Research (DZD), Ingolstädter Landstrasse 1, 85764 Neuherberg, Germany
[9]Lead Contact
*Correspondence: bruening@sf.mpg.de
https://doi.org/10.1016/j.neuron.2020.04.020

SUMMARY

Melanin-concentrating hormone (MCH)-expressing neurons are key regulators of energy and glucose homeostasis. Here, we demonstrate that they provide dense projections to the median eminence (ME) in close proximity to tanycytes and fenestrated vessels. Chemogenetic activation of MCH neurons as well as optogenetic stimulation of their projections in the ME enhance permeability of the ME by increasing fenestrated vascular loops and enhance leptin action in the arcuate nucleus of the hypothalamus (ARC). Unbiased phosphoRiboTrap-based assessment of cell activation upon chemogenetic MCH neuron activation reveals MCH-neuron-dependent regulation of endothelial cells. MCH neurons express the vascular endothelial growth factor A (VEGFA), and blocking VEGF-R signaling attenuates the leptin-sensitizing effect of MCH neuron activation. Our experiments reveal that MCH neurons directly regulate permeability of the ME barrier, linking the activity of energy state and sleep regulatory neurons to the regulation of hormone accessibility to the ARC.

INTRODUCTION

The median eminence (ME) as a circumventricular organ plays a major role as a blood-brain barrier (BBB)-permeable site between the periphery of the organism and the central nervous system (CNS). First, it is the site where neuronal axon terminals release secreted peptides and transmitters into the portal capillary system (Clarke, 2015). Second, it can transport blood-borne signals to their target regions in the brain (Martínez et al., 2019; Schaeffer et al., 2013). The key structures of this barrier are composed of tanycytes and fenestrated microvessel loops (Prevot et al., 2018). Tanycytes are unique cell types, which are specialized ependymal cells lining the floor of the third ventricle. They elongate single and long basal processes to either the external part of the ME or into the neighboring brain tissue, such as the mediobasal hypothalamus (Mullier et al., 2010). Another functionally important compartment of the ME is formed by a network of fenestrated capillary loops (Ciofi et al., 2009). These long loops are mainly surrounded by ME tanycyte termi-

nals and neurosecretory endings of neuroendocrine neurons. This discrete structure makes the ME stand out as an important gate for "brain-peripheral crosstalk." In previous studies, it was found that the ME undergoes feeding-state-dependent-plasticity by tanycyte-derived vascular endothelial growth factor A (VEGFA) release (Langlet et al., 2013). However, this model leaves open the question of whether internal-state-dependent modulation of neurons may also, in turn, contribute to state-dependent regulation of ME barrier plasticity.

Interestingly, two recent studies showed that melanin-concentrating hormone (MCH)-expressing neurons through projection sites around the third ventricle regulate the flow of the cerebrospinal fluid (CSF) and feeding behavior (Conductier et al., 2013; Noble et al., 2018). MCH neurons are distributed exclusively in the lateral hypothalamus (LH) and the zona incerta (ZI) of the brain (Bittencourt, 2011). Abundant experiments, i.e., either intracerebroventricular (i.c.v.) injection of MCH or overexpression and knockout of MCH, all point toward a critical regulatory function of MCH neurons in the integrated control of food
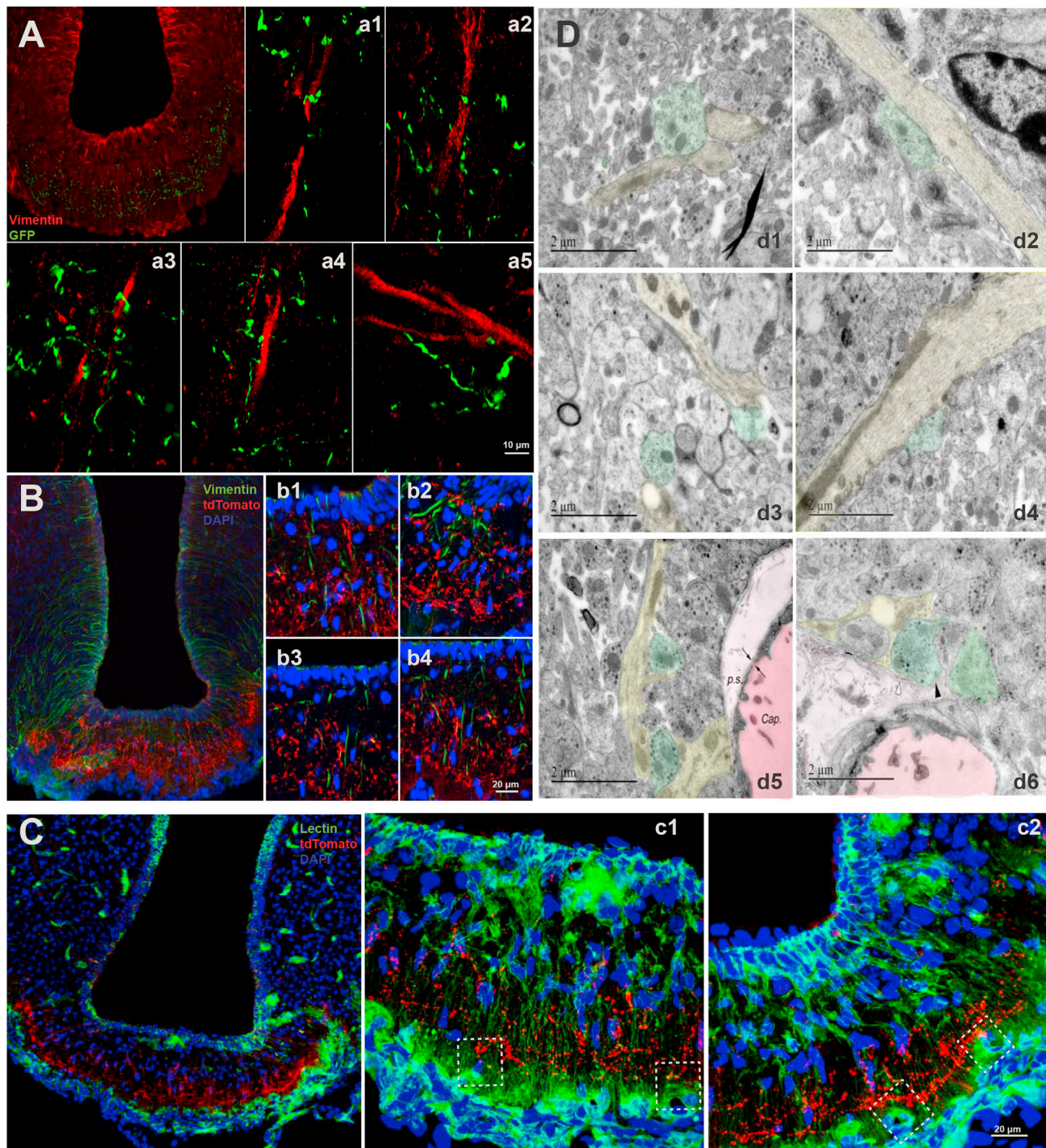
Figure 1. MCH Neuron Projections in the ME

(A) Immunohistochemistry using anti-Vimentin (red) and anti-GFP antisera (green) in ARC/ME sections of ChR2-eYFP[MCH] mice; (a1)–(a)5 show enlarged exemplary regions from the ME region depicted in (A).

(B) Immunohistochemistry using anti-Vimentin (green) and anti-tdTomato (red) in ARC/ME sections of Synaptophysin-tdTomato[MCH] mice; (b1)–(b4) show enlarged exemplary regions from the ME region depicted in (B).

(C) Immunohistochemistry using lectin (green) and anti-tdTomato (red) in ARC/ME sections of Synaptophysin-tdTomato[MCH] mice; (c1) and (c2) show enlarged exemplary regions from the ME region depicted in (C). Dashed white square in (c1) and (c2) show the close contact between lectin-positive vessels and MCH neuron terminals.

(legend continued on next page)

intake, locomotor activity, and systemic glucose homeostasis (Hausen et al., 2016; Ludwig et al., 2001; Macneil, 2013; Rossi et al., 1997). Besides their role in the control of energy homeostasis, electrophysiological recordings of MCH neurons across sleep cycles and specific optogenetic manipulation of MCH neurons revealed that MCH neurons were firing more actively during rapid eye movement (REM) sleep cycles (Hassani et al., 2009) and through different projection sites across the brain, MCH neuron activation increased REM sleep (Konadhode et al., 2013). Collectively, these studies define the MCH neurocircuitry as a highly interconnected system within and beyond the hypothalamus (Diniz and Bittencourt, 2017; Komagata et al., 2019), integrating the regulation of energy homeostasis and sleep.

Here, we identify dense projections of MCH neurons from the LH and ZI to the ME region. These findings provoked the question of whether MCH neurons may modulate the ME barrier contributing to the regulation of blood-borne hormone accessibility to the hypothalamus and, thus, may have broader effects on metabolic control. By using several transgenic mouse lines for visualization as well as chemogenetic and optogenetic activation of MCH neurons, we demonstrate that these integral regulators of metabolism and sleep also control the accessibility of the mediobasal hypothalamus for blood-borne signals, as exemplified by leptin. Thus, our study adds an important mechanism to the action of MCH neurons in the regulation of energy homeostasis besides classical synaptic as well as volume transmission.

RESULTS

MCH Neurons Provide Dense Projections to the ME and Closely Contact Tanycytes and Fenestrated Capillaries

To investigate the projection patterns of MCH neurons, we used two different MCH neuron reporter mouse lines. First, we generated mice, which express channelrhodopsin 2 (ChR2) fused to enhanced yellow fluorescent protein (eYFP) in MCH neurons including their projections by crossing MCH^{Cre} mice with those allowing for Cre-dependent expression of ChR2-eYFP from the ROSA26 locus. Here, we found that ChR2-eYFP-marked MCH neuron projections were readily detected in the ME (Figure 1A; Figure S1). To visualize whether there were potential contacts between MCH neuron projections and tanycytic processes, we performed double immunolabeling for eYFP and vimentin in ME sections from ChR2-eYFP^{MCH} mice. Indeed, MCH neuron terminals closely contact tanycytic processes, as resolved by confocal microscopy (Figure 1A). To investigate whether these projections from MCH neurons represented synaptic terminals, we crossed MCH^{Cre} mice with animals, which allowed for Cre-dependent expression of a synaptophysin-tdTomato fusion pro-

tein from the ROSA26 locus. Here, immunostaining for tdTomato allowed visualization of synaptic vesicles in presynaptic sites of MCH neurons. Coimmunolabeling for synaptophysin-tdTomato and vimentin confirmed abundant MCH neuron terminals in close proximity to tanycyte processes (Figure 1B).

To define potential structural contacts between MCH neuron projections and another important component of the ME, i.e., fenestrated capillary loops, double-labeled staining for lectin-marked vascular cells and tdTomato in Synaptophysin-tdTomato^{MCH} mice showed that, in the external region of the ME, MCH neuron synaptic terminals were densely distributed in close proximity to capillary loops (Figure 1C).

Due to the resolution limitations of confocal microscopy, we could not further define the exact structural contacts between MCH neurons and ME structures by using this technology. To further address this question, we performed electron microscopy (EM) for visualization of the ultrastructural contacts of MCH neurons and ME components. Here, we found that MCH neuron terminals, which contained silver-amplified highly electron-dense particles by immunolabeled tdTomato staining of Synaptophysin-tdTomato^{MCH} mice, were indeed closely located around tanycytic processes in the ME (Figure 1D). In addition, in the external zones of the ME, MCH neurons had terminals, which were close to the pericapillary space (Figure 1D, d5) and even contacted the parenchymatous basal lamina (Figure 1D, d6).

Collectively, MCH neurons provide projections to the ME and have close structural contact with both tanycytic processes and the vascular wall containing the fenestrated capillaries. These anatomical findings indicate a potential functional interaction of MCH neurons with key components of the ME in control of ME barrier permeability.

Chemogenetic Activation of MCH Neurons Increases Permeability of the ME Barrier and Promotes Increased Fenestration of Microvessels

Previous studies had shown that fasting induces increased fenestration of ME microvessel loops to the arcuate nucleus of the hypothalamus (ARC) and tight-junction-complex reorganization of tanycytes in the ARC (Langlet et al., 2013). To address whether the observed structural contacts of MCH neurons with critical barrier components in the ME could functionally alter the permeability of the ME barrier, we investigated the effect of chemogenetic activation of these neurons on ME barrier permeability. To this end, mice that allowed for chemogenetic activation through transgenic expression of the activatory DREADD (Designer Receptors Exclusively Activated by Designer Drugs) receptor hM3Dq in MCH neurons (hM3Dq^{MCH} mice) were injected with 1% Evans blue dye into the tail vein to mimic access of peripheral signals to the ARC through the ME barrier.

(D) Electron microscopy of the ME sections in Synaptophysin-tdTomato^{MCH} mice. Tanycytic processes are marked in yellow, as defined by their elongated mitochondria; the presence of electron-dense cytoskeletal bundles as well as glycogen storage and MCH nerve terminals are marked in green that contain silver-amplified highly electron-dense particles (d1–d4). (d5) and (d6) taken from external zone of ME, where neuroendocrine terminals reach close proximity to the pericapillary space (p.s., light pink) of the pituitary portal vessel (dark pink) capillary plexus (Cap.). The two arrows in the bottom left panel show a fenestration in the endothelium. In (d6), the black arrowhead shows a tomato-immunoreactive nerve terminal (green) contacting the parenchymatous basal lamina delineating the pericapillary space; the white arrowhead shows a thin tanycytic process (yellow) inserted between the MCH nerve terminal (green) and the basal lamina. Scale bars: 10 μm in (A), 20 μm in (B), 20 μm in (C), and 2 μm in (D).
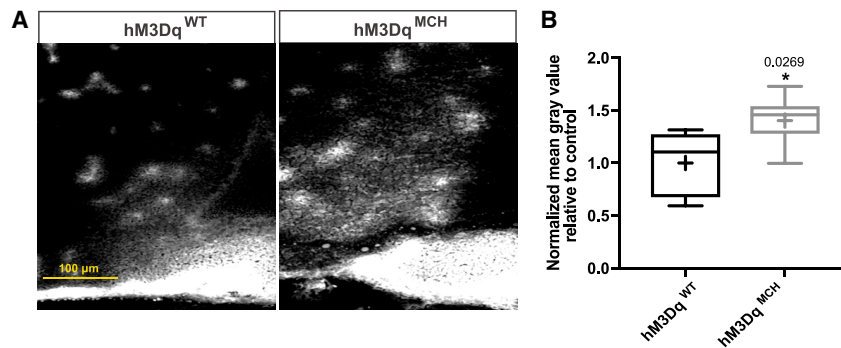
Figure 2. Chemogenetic Activation of MCH Neurons Enhances the Permeability of the ME Barrier

(A) Representative images of Evans blue dye diffusion into the ARC region of fasted and 4-h CNO-injected control and hM3Dq^{MCH} mice.

(B) Quantification of Evans blue dye diffusion upon CNO treatment of control (n = 5) and hM3Dq^{MCH} mice (n = 7). Bar graphs represent the min to max value, the mean value is marked as "+". Statistical analysis: unpaired Student's t test, *p < 0.05.

Analysis of dye distribution in the ARC revealed that activation of MCH neurons evoked a clear enhancement of Evans blue diffusion in the ARC compared to fasted and 4-h clozapine-N-oxide (CNO)-treated control mice, which did not express the DREADD receptor (hM3Dq^{WT}) (Figures 2A, 2B, and S1). Importantly, Evans blue diffusion did not differ between vehicle-treated hM3Dq^{MCH} and hM3Dq^{WT} mice, further supporting that the observed increase in ME permeability was the specific result of chemogenetic MCH neuron activation (Figures S2A and S2B).

To investigate whether the observed changes in ME permeability represent a direct consequence of MCH neuron activation or may occur secondarily to metabolic changes induced by MCH neuron stimulation, we determined circulating insulin, leptin, ghrelin, and corticosterone concentrations as well as performed insulin and glucose tolerance tests in CNO-treated hM3Dq^{MCH} and hM3Dq^{WT} mice. These analyses revealed no changes in circulating energy-state-sensing hormones between the two groups of mice (Figures S3A–S3D). Similarly, chemogenetic MCH neuron activation had no effect on insulin sensitivity and glucose tolerance (Figures S3E and S3F). Taken together, the results show that the observed increase in ME permeability upon chemogenetic MCH neuron activation occurred in the absence of major metabolic alterations.

To investigate whether this increase in ME barrier permeability as a consequence of activating MCH neurons was accompanied by structural changes of the ME barrier, we then examined two key structures underlying this regulation, i.e., the quantity of fenestrated microvessel loops, as assessed by immunohistochemical staining for MECA-32, and the formation of tanycyte tight-junction-complexes, as assessed via ZO-1 immunohistochemistry. We found a clear increase of MECA-32-marked fenestrated microvessel loops in CNO-treated hM3Dq^{MCH} mice compared to CNO-treated control animals in both the ARC and ME (Figures 3A and 3B). In contrast, there were no differences detectable in ZO-1-marked tight junction complexes, which exhibited the classical honeycomb-like pattern of organization in the ventromedial ARC (Figures 3A and 3C). Together, these findings indicate that activation of MCH neurons promotes increased ME permeability and that this effect is accompanied by structural alterations of fenestrated capillaries in the ME and the ARC.

To further investigate the structural alterations of microvessels in the ARC upon chemogenetic MCH neuron activation, we assessed the fenestration of ME microvessel loops reaching the ventromedial ARC directly by EM-based imaging. This analysis revealed a clear enhancement of microvessel loop fenestration upon chemogenetic MCH neuron activation (Figures 3D–3F).
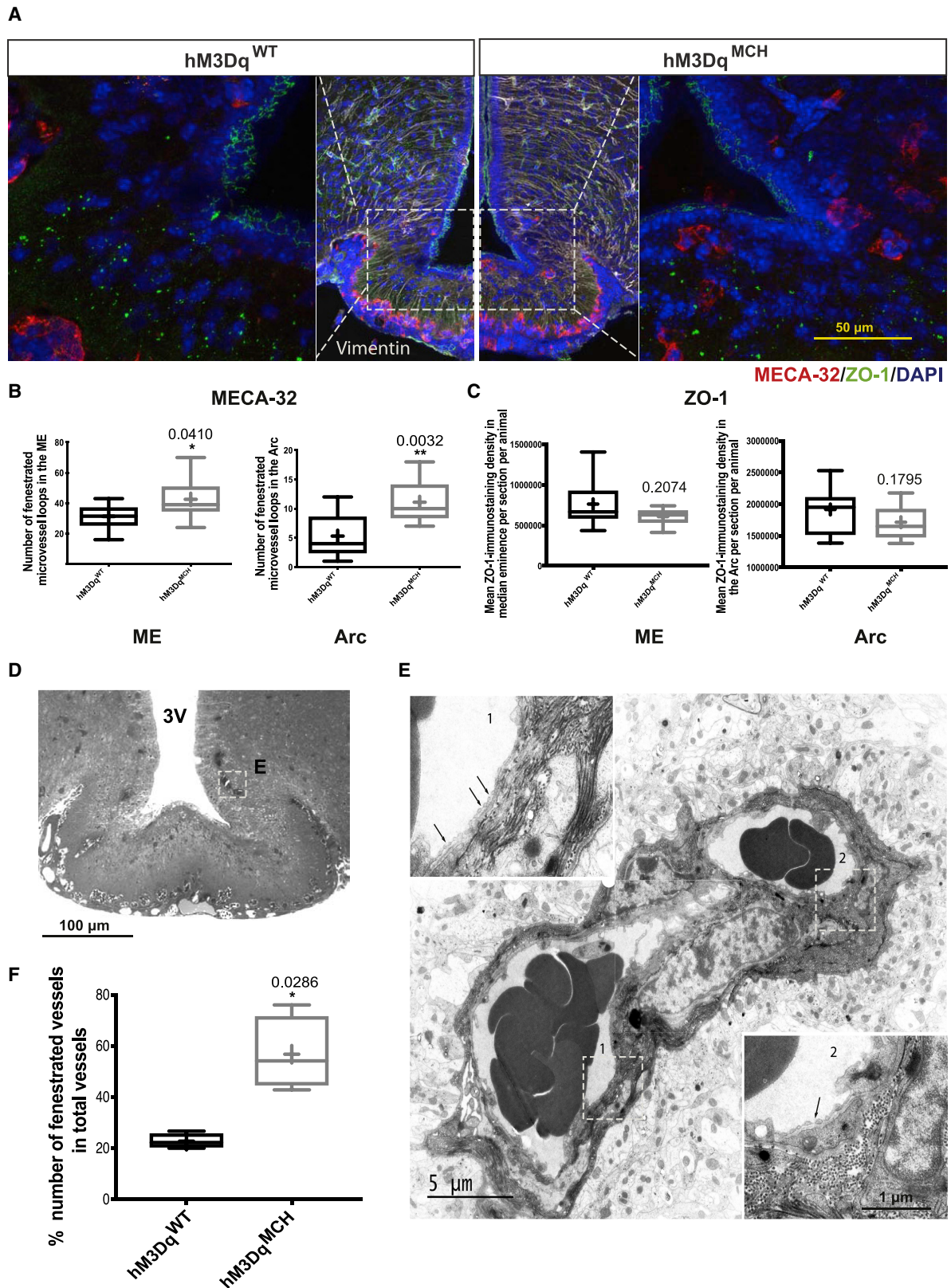
Taken together, our results reveal that chemogenetic MCH neuron activation enhances microvessel fenestration in the ME and the ARC.

Chemogenetic Activation of MCH Neurons Increases Leptin Action

To test whether the MCH-neuron-dependent changes in ME structure and permeability potentially also translate into an altered ability of energy-state-sensing hormones to access the ARC, we next performed leptin sensitivity experiments in hM3Dq^{MCH} mice and control littermates. Both groups of animals were treated with CNO 4 h before an intraperitoneal (i.p.) injection of vehicle or leptin. CNO administration upon subsequent vehicle treatment in 16-h fasted hM3Dq^{MCH} mice resulted in an increase in food intake upon refeeding compared to control mice (Figure S4A). These findings are consistent with previous studies revealing increased food intake upon chemogenetic activation of MCH neurons (Noble et al., 2018). However, this effect was not detectable after 4 h of refeeding (Figure S4B).

Next, we investigated the food intake suppressive effect of a single i.p. injection of leptin in CNO-treated hM3Dq^{MCH} mice and control littermates. Interestingly, following chemogenetic activation of MCH neurons upon CNO treatment of hM3Dq^{MCH} mice, leptin suppressed food intake after 1 h of refeeding compared to saline-treated animals, whereas this effect was absent in CNO-treated control animals receiving the same dose of peripherally applied leptin (Figure 4A). Calculating the ratio of food intake suppression upon leptin treatment versus saline treatment within each group of animals revealed that leptin-induced suppression of 1 h of food intake was more pronounced in hM3Dq^{MCH} than in control animals (Figure 4B). However, this effect was not detectable 4 h after leptin application, indicating that chemogenetic MCH neuron activation predominantly enhanced the rapid induction of leptin-induced feeding suppression, consistent with the increase in ME permeability, thus facilitating rapid access of leptin to the ARC (Figures S4B and S4C).

To investigate leptin-induced signaling in the ARC on a molecular level, we assessed the dynamics of the ability of leptin to evoke STAT3 phosphorylation (pSTAT3) under the same

A

B MECA-32

C ZO-1

D

E

F

(legend on next page)

A

B

C

15 min Leptin stimulation

D
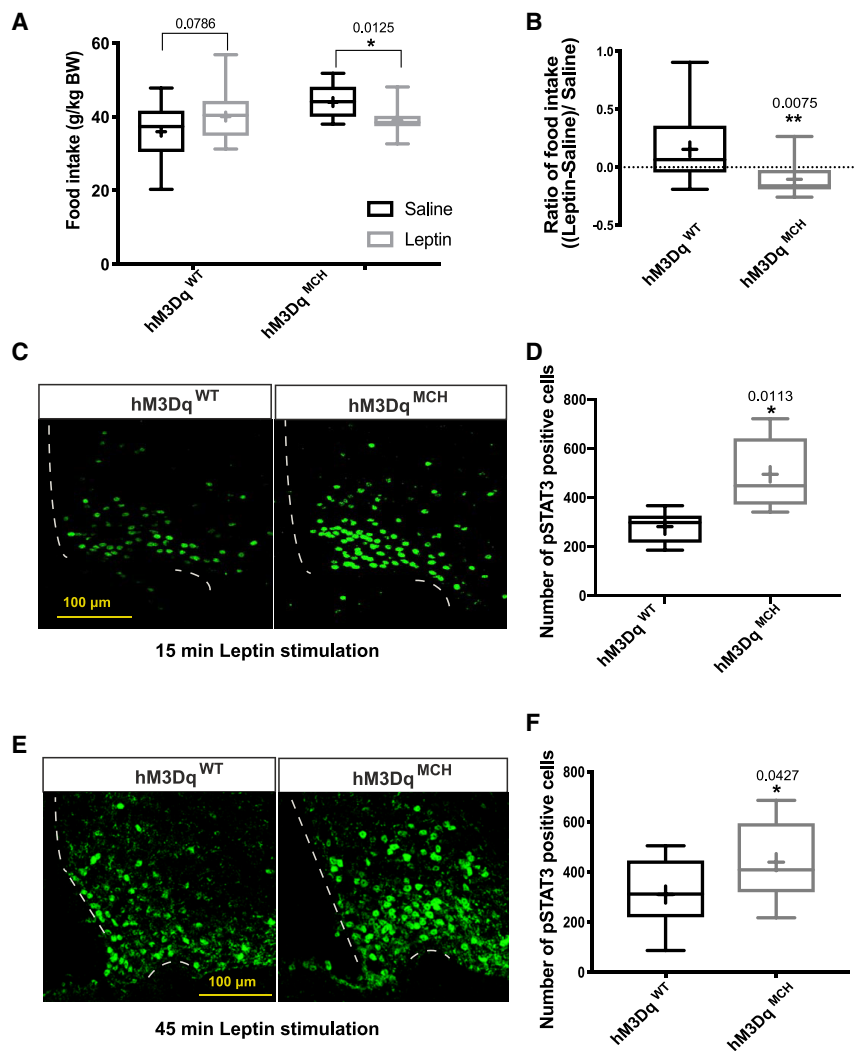

E

45 min Leptin stimulation

F

Figure 4. Chemogenetic Stimulation of MCH Neurons Promotes Leptin Action

(A) Assessment of leptin sensitivity by comparing the effect of saline or leptin injection on 1-h refeeding food intake in CNO-treated control (n = 16) and hM3Dq^{MCH} mice (n = 13).

(B) The ratio of (food intake in leptin treated condition–food intake in saline treated condition)/ food intake in saline-treated condition in CNO-treated control (n = 16) and hM3Dq^{MCH} mice (n = 13).

(C) Representative image of pSTAT3 immunoreactivity in CNO-treated control and hM3Dq^{MCH} mice with 15-min leptin stimulation.

(D) Quantification of the number of pSTAT3-positive cells in the ARC of 15-min leptin-injected, fasted, and CNO-treated control (n = 6) and hM3Dq^{MCH} mice (n = 5).

(E) Representative image of pSTAT3 immunoreactivity in CNO-treated control and hM3Dq^{MCH} mice with 45-min leptin stimulation.

(F) Quantification of the number of pSTAT3-positive cells in the ARC of 45-min leptin-injected, fasted, and CNO-treated control (n = 12) and hM3Dq^{MCH} mice (n = 13). Bar graphs represent the min to max value, the mean value is marked as "+". Statistical analysis: unpaired Student's t test, *p < 0.05, **p < 0.01, except leptin sensitivity where a paired Student's t test was used, *p < 0.05.

Optogenetic Activation of MCH Neuron Projections in the ME Enhances ME Permeability and Leptin Sensitivity

Because chemogenetic activation of MCH neurons promotes the release of MCH and other peptides and neurotransmitters from these neurons across the broad neurocircuitry targeted by these cells, our previous experiments left open

experimental conditions. Here, leptin treatment lead to an enhanced activation of pSTAT3 in the ARC upon previous chemogenetic activation of MCH neurons as early as 15 min after leptin injection, and this effect of enhanced leptin-evoked STAT3-phosphorylation remained increased 45 min after leptin application (Figures 4C–4F).

In summary, chemogenetic activation of MCH neurons increases ME barrier permeability and enhances the ability of leptin to rapidly activate STAT3 phosphorylation in the ARC and to acutely suppress feeding.

the question about the contribution of MCH neuron-ME projections in the regulation of ME permeability and leptin action. To address this question, we aimed at selectively targeting the MCH neuron-ME projections by optogenetic activation. Therefore, we implanted optical fibers into the third ventricle just above the ME of ChR2-tdTomato^{MCH} and control animals (Figure S5A). Blue light illumination of MCH neuron-ME projections (10 Hz) did not affect subsequent food intake upon vehicle injection in a refeeding paradigm when comparing ChR2-tdTomato^{MCH} and control animals (Figure S5B). To investigate whether the

---

Figure 3. Chemogenetic Activation of MCH Neurons Enhances the Permeability of the ME Barrier through Increased Fenestration of Microvessel Loops

(A) Representative images of anti-MECA-32 (red), anti-tight-junction-1 (ZO-1, green), and anti-Vimentin (white) immunoreactivity in the ME region. The left image shows a hemisection of a CNO-treated control animals and the right show a hemisection of a CNO-treated hM3Dq^{MCH} mouse.

(B and C) Quantification of number of MECA-32-marked microvessel loops (B) d and ZO-1-marked tight junction complexes (C) in both the ME and the ARC region of fasted and CNO treatment of control (n = 6–10) and hM3Dq^{MCH} mice (n = 9–11).

(D) Light microscopy image showing the capillaries illustrated in (E) (white square) in a 1-μm-thick semithin section.

(E) Representative electron microscopy image showing two fenestrated capillaries (see fenestrae shown by arrows in insets 1 and 2) in the ventromedial ARC of a CNO-treated hM3Dq^{MCH} mice.

(F) Quantification of capillary fenestration upon fasted and CNO-treated control (n = 4) and hM3Dq^{MCH} mice (n = 4). Bar graphs represent the min to max value, the mean value is marked as "+". Statistical analysis: unpaired Student's t test, *p < 0.05.
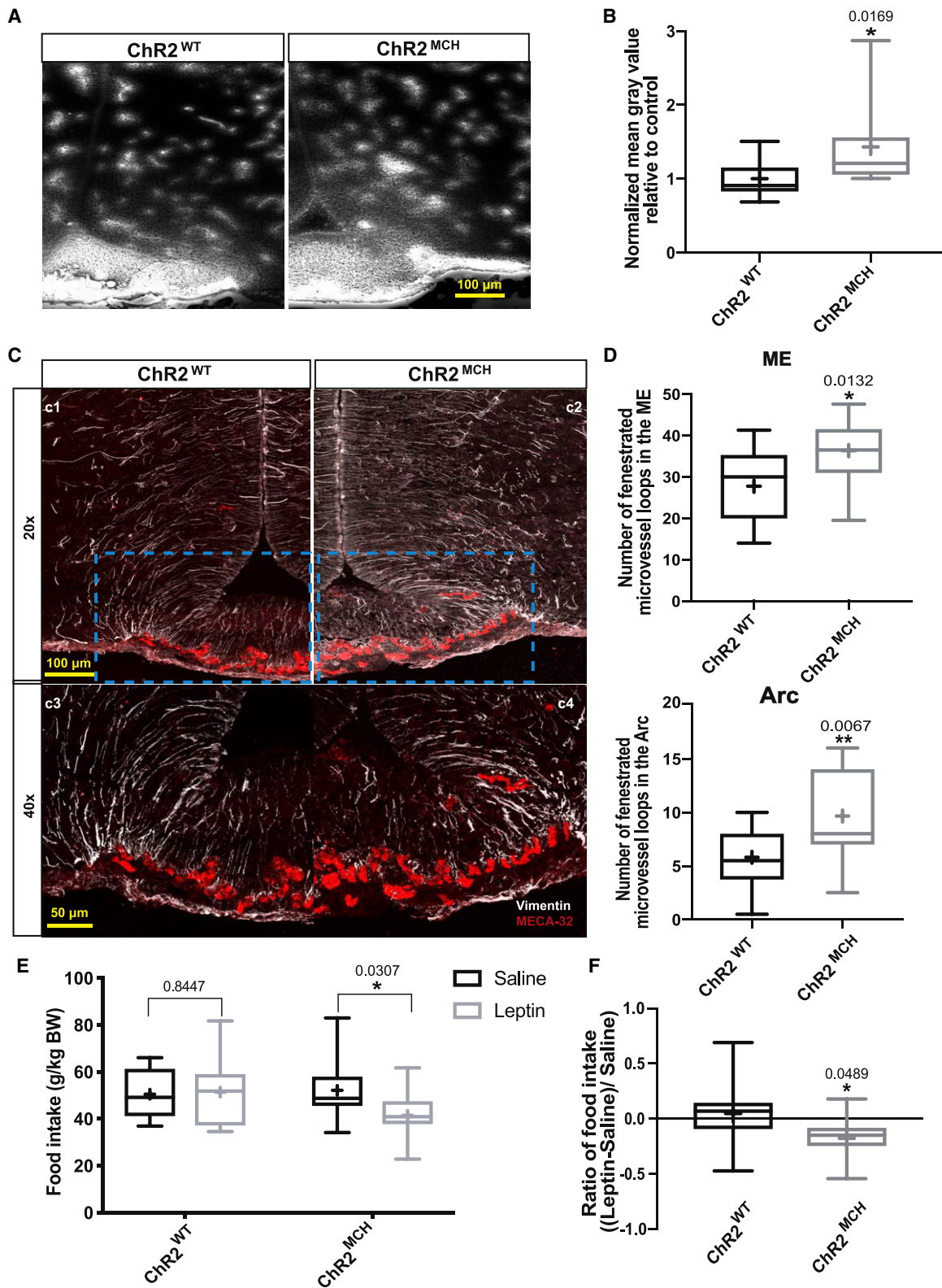
Figure 5. Optogenetic Stimulation of MCH-ME Projections Promotes Leptin Action

(A) Representative images of Evans blue dye diffusion into the ARC region of fasted and 3.5-h blue-light-illuminated control and ChR2[MCH] mice.

(B) Quantification of Evans blue dye diffusion upon blue light illuminated of control (n = 14) and ChR2[MCH] mice (n = 12).

optogenetic fiber implantation potentially interferes with the ability of MCH neuron activation to increase the rapid refeeding response, we investigated the food intake stimulatory effect of chemogenetically activating MCH neurons in hM3Dq^{MCH} and hM3Dq^{WT} mice, which had been implanted with optical fibers in the same position as ChR2-tdTomato^{MCH} mice. This analysis revealed that fiber implantation did not interfere with the ability of chemogenetically activating MCH neurons to increase the rapid refeeding response (Figures S5C and S5D).

However, when we stimulated MCH neuron-ME projections in ChR2-tdTomato^{MCH} mice, this intervention enhanced Evans blue diffusion in the ME (Figures 5A and 5B) as well as increased the number of fenestrated microvessel loops in the ME and the ARC (Figures 5C and 5D). Moreover, optogenetic stimulation of MCH neuron-ME projections in ChR2-tdTomato^{MCH} mice enhanced the leptin-induced suppression of 1-h refeeding in ChR2-tdTomato^{MCH} mice but not in control animals (Figures 5E and 5F). The control mice did not show a significant response to a single peripheral application of leptin at both time points after refeeding (Figures 5E and 5F; Figure S5F).

Collectively, these experiments indicate that the ability of MCH neuron activation to increase the permeability of ME microvessel loops reaching the ventromedial ARC and leptin's anorexigenic action was indeed mediated by MCH neuron-ME projections, whereas the food-intake-stimulatory effect of chemogenetic MCH neuron activation was likely due to an increased access of orexigenic hormones, such as ghrelin, to the ARC or to alternative mechanisms governed by MCH neurons, which is in line with previous reports.

MCH Does Not Modulate Tanycyte Signaling

MCH is one of main peptides released from MCH neurons and also has been extensively investigated with regard to its regulatory role in energy homeostasis. Given the effects of chemogenetic and optogenetic MCH neuron stimulation on ME barrier permeability and leptin action, we speculated that MCH may directly act on tanycytes and fenestrated capillaries. To this end, first we established in-vitro-purified tanycyte cultures as a model to test the potential effects of MCH on these cells. However, we found that mRNA expression of the MCH receptor 1 (MCHR1) is relatively low in sorted tanycytes compared to other cells in the ME region (Figure S6A). Similarly, in situ hybridization by RNA scope revealed that MCHR1 mRNA was barely expressed in tanycytes (Figure S6B). Moreover, by incubating tanycyte cultures with MCH, we failed to detect activation of ERK or AKT signaling in these cells (Figures S6C and S6D). It is well known that MCH through activation of MCHR1 suppresses forskolin-stimulated cyclic AMP (cAMP) concentrations and increases intracellular Ca^{2+} (Pissios et al., 2003). Therefore,

we tested whether MCH incubation of tanycytes can regulate cAMP levels. Similar to what was observed for ERK and AKT signaling, we found that MCH incubation did not affect cAMP concentrations in tanycytes (Figure S6E). Together, these findings show that MCH does not affect signaling in cultured tanycytes.

However, to exclude other signaling pathways that may be involved in the MCH regulatory role of tanycytes, we used Ca^{2+} imaging in living brain slices containing the ME, which allowed us to directly visualize calcium activity on different cell types in the ME (Figure S6F). Nevertheless, we found that MCH peptide application onto the ME slices did not induce any changes in intracellular Ca^{2+} compared to a negative control (artificial cerebrospinal fluid [ACSF] treatment), whereas ATP evoked clear increases in intracellular Ca^{2+} in the different cell types in the ME (ARC-tanycytes/ME-tanycytes/vessels of the pars tuberalis/blood vessels below the ME) (Figure S6G). Finally, considering that MCH neurons in addition to MCH can also release glutamate or GABA, we next tested the potential effect of both transmitters on Ca^{2+} activity of the ME slices. However, either incubating slices with the glutamate receptor ligand glutamate (G162, Sigma, 100 μM) or the GABA receptor agonist baclofen (0417, Tocris, 1 mM) failed to elicit changes in intracellular Ca^{2+} concentrations in tanycytes (Figure S6H). Hence, our data argue that MCH does not modulate signaling of the classical MCH-regulated pathways in tanycytes and capillaries in the ME.

MCH Neurons Regulate Endothelial Cells in the ME

Given that stimulation of MCH neurons alters ME permeability by increasing fenestrated vessel loops and that, specifically, MCH neuron-ME projections regulate these effects, we aimed to further investigate the mechanisms underlying this regulation. Thus, we performed phosphoRiboTrap experiments to explore the nature of the cell types in the ME regulated as a consequence of chemogenetically activating MCH neurons. In previous studies, it was shown that phosphorylation of the ribosomal protein S6 as a bona fide target of mTOR signaling well reflects cell activation in response to a wide array of stimuli (Knight et al., 2012). The method builds on the fact that the S6 ribosomal protein is activated in cells upon activation of tyrosine kinase and G-protein-coupled receptor signaling. Thus, precipitation of S6-marked ribosomes and sequencing of associated mRNAs allows for the unbiased identification of cell types, in which mTOR signaling was modulated upon a defined stimulus. To identify cell types that exhibit altered mTOR signaling upon chemogenetic MCH neuron activation, fasted hM3Dq^{MCH} and control littermates (hM3Dq^{WT}) were injected with CNO (3 mg/kg i.p.). Mice were sacrificed 1 h after CNO injection. The ARC and ME region was dissected and subjected to

---

(C) Representative images of anti-MECA-32 (red) and anti-Vimentin (white) immunoreactivity in the ME region. The left image (c1) shows a left hemisection of a blue-light-illuminated control mouse, and the right images shows (c2) a right hemisection of a blue-light-illuminated ChR2^{MCH} mouse. Bottom panel shows the magnified images (c3 and c4) from (c1) and (c2).

(D) Quantification of the number of MECA-32-marked microvessel loops in both the ME and the ARC region of blue-light-illuminated control (n = 17) and ChR2^{MCH} mice (n = 11).

(E and F) Same comparison of leptin sensitivity as depicted in Figure 4A and 4B, upon blue-light-illumination above the ME of control (n = 12) and ChR2^{MCH} mice (n = 11). Bar graphs represent the min to max value, the mean value is marked as "+". Statistical analysis: unpaired Student's t test, *p < 0.05, **p < 0.01, and ***p < 0.001, except leptin sensitivity comparison by paired Student's t test, *p < 0.05.

A

B

C

Cluster 0

Cluster 1

Cluster 2

Cluster 3
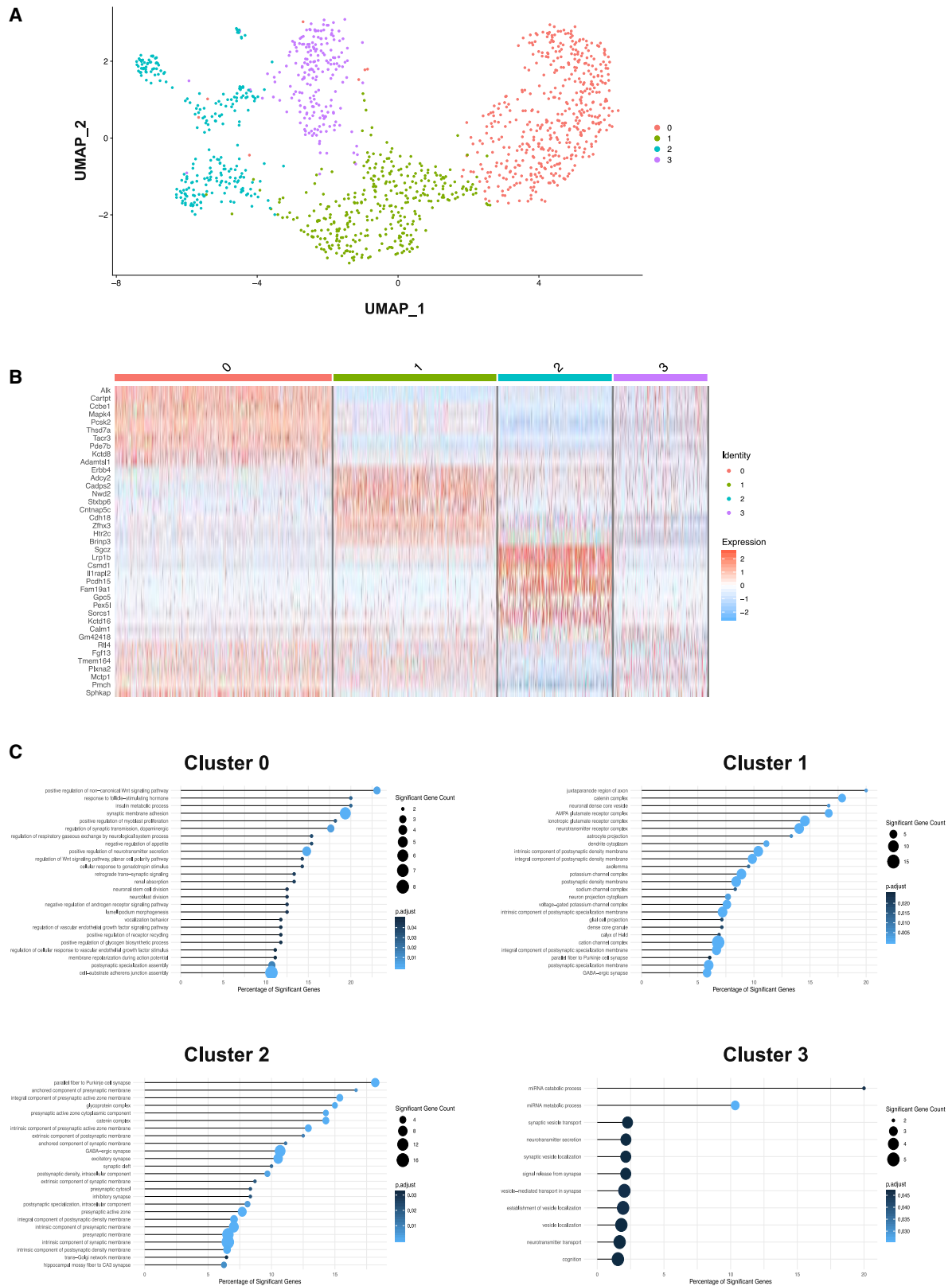
(legend on next page)

immunoprecipitation with an anti-pS6 antibody to immunopurify ribosomes from cell types, where mTOR signaling was altered as a consequence of chemogenetic MCH neuron activation. After RNA extraction, both input RNA and that associated with immunoprecipitated (IP) ribosomes were subjected to deep mRNA sequencing in both groups of mice. By comparing the reads in the IP/input ratio, we were able to identify gene clusters, which were enriched in the ribosomes of cell types, which had undergone alterations of mTOR signaling in response to MCH neuron activation (Table S1). When we analyzed the overlap of genes enriched in the IP/input of MCH-neuron-activated mice with that of previously identified cell types by using unbiased droplet-based single-cell mRNA sequencing of cells in the mediobasal hypothalamus (Campbell et al., 2017), we identified gene clusters that represented neurons and glial cells, as well as endothelial cells, whose transcripts exhibited an enrichment in the IPs from MCH-neuron-activated mice (Figures S7A and S7B). Collectively, MCH neuron activation among other cell types alters mTOR signaling in endothelial cells of the ME/ARC.

MCH Neurons Express VEGFA and Modulate Leptin Sensitivity in a VEGFA-Dependent Manner

To define the mechanisms through which MCH neuron activation may regulate endothelial cell signaling and increases fenestration of vessel loops in the ME, we aimed to identify potential signals originating from MCH neurons and capable of regulating endothelial function. To this end, we performed single-nucleus RNA sequencing of MCH neurons, which were subjected to fluorescence-activated cell sorting (FACS) upon MCH-neuron-specific ZsGreen expression in ZsGreen[MCH] mice. Using this approach, we obtained single-nuclei mRNA sequencing reads from 1,266 isolated MCH neurons. An analysis of gene expression revealed the identification of previously unrecognized heterogenous cell clusters of MCH neurons (Figures 6A and 6B). These 4 clusters of MCH neurons were characterized by the expression of distinctive mRNAs (Table S2). We clustered the 1,266 cells using the R Seurat package (Butler et al., 2018) (version 3.1.1). A small cluster_resolution parameter of 0.2 ensures grouping of the cells into few clusters. The resulting marker genes for each clusters were then used as input for a Gene Ontology (GO) term analysis by using the R clusterProfiler package (Yu et al., 2012) (version 3.14.3). To avoid redundant GO terms, we used clusterProfiler's simplify function with default parameters. The significantly regulated simplified GO terms are then sorted by rich factor, which is determined by rich factor = (significant gene count of GO term)/(total gene count of GO term). This analysis identified specific GO terms enriched in the 4 clusters of MCH neurons (Figure 6C). Interestingly, genes defining the largest cluster of MCH neurons (cluster 0) exhibited an enrichment of genes in the GO term "regulation of

VEGF signaling pathway" and GO term "positive regulation of endothelial cell proliferation." This lead us to specifically investigate the expression of VEGFA, which has been previously found to critically regulate the ME barrier (Langlet et al., 2013), across the different clusters of MCH neurons. This analysis revealed that VEGFA mRNA was indeed expressed across the different clusters of MCH neurons (Figure S7C).

To further validate VEGFA expression in MCH neurons, we used RNAscope-based *in situ* hybridization for *VEGFA* mRNA expression in tdTomato[MCH] mice. Here, we confirmed *VEGFA* mRNA expression in MCH neurons (Figure 7A). In addition, immunostaining was performed for visualizing VEGFA protein expression in genetically marked MCH neurons of tdTomato[MCH] reporter mice. This analysis revealed a clear overlay of VEGFA immunoreactivity and tdTomato immunoreactivity in MCH neurons of the lateral hypothalamic area (LHA) (Figure 7B). Comparing the percentage of VEGFA-positive MCH neurons to that of non-MCH neurons in the LHA revealed an enrichment of VEGFA-expressing neurons in MCH compared to non-MCH neurons (Figure 7C). Collectively, several independent lines of experimental evidence revealed the expression of VEGFA in MCH neurons.

To test whether VEGFA signaling contributes to the MCH-neuron-activity-dependent regulation of ME permeability, we investigated the ability of MCH neuron activation to regulate leptin sensitivity upon pharmacological inhibition of VEGFA signaling. Pretreatment with the VEGFR blocker Axitinib attenuated the ability of chemogenetic MCH neuron activation to enhance the anorexigenic effect of peripherally applied leptin (Figure 7D). Collectively, these data indicate that, at least in part, MCH-neuron-dependent VEGFA signaling contributes to the enhancement of leptin's acute anorexigenic effect upon chemogenetic MCH neuron activation.

DISCUSSION

The maintenance of energy homeostasis requires the rapid transfer of energy-state-sensing signals from the periphery of the organism to the CNS. The characteristics of the ME barrier in immediate anatomical proximity to the hypothalamus play a key role in this process. Previous work had indicated not only that the concentration of these energy-state-communicating signals varies upon changes in internal state but also that ME barrier function is modulated in response to fasting (Langlet, 2013, 2019; Varela and Horvath, 2012). Our results unravel a previously unrecognized mechanism through which the activity of neurons in the hypothalamus, which are regulated during sleep and implied in control of energy homeostasis, in turn regulates vascular fenestration in the ME to enhance barrier permeability and further hormone access in a VEGFA-dependent manner.

Figure 6. Single-Nucleus Sequencing of MCH Neurons
(A) Heterogenous cell clusters of MCH neurons based on single-nucleus sequencing from ZsGreen[MCH] reporter mice.
(B) Heatmap of cell clusters with marker genes of MCH neurons. Color code on the top same as (A). Color scale indicates gene expression level.
(C) Gene Ontology (GO) term analysis of each MCH cell cluster. GO term significance mapped to color. Percentage of significant genes depicts the ratio of significant genes in GO term to all genes defining the term in percent.
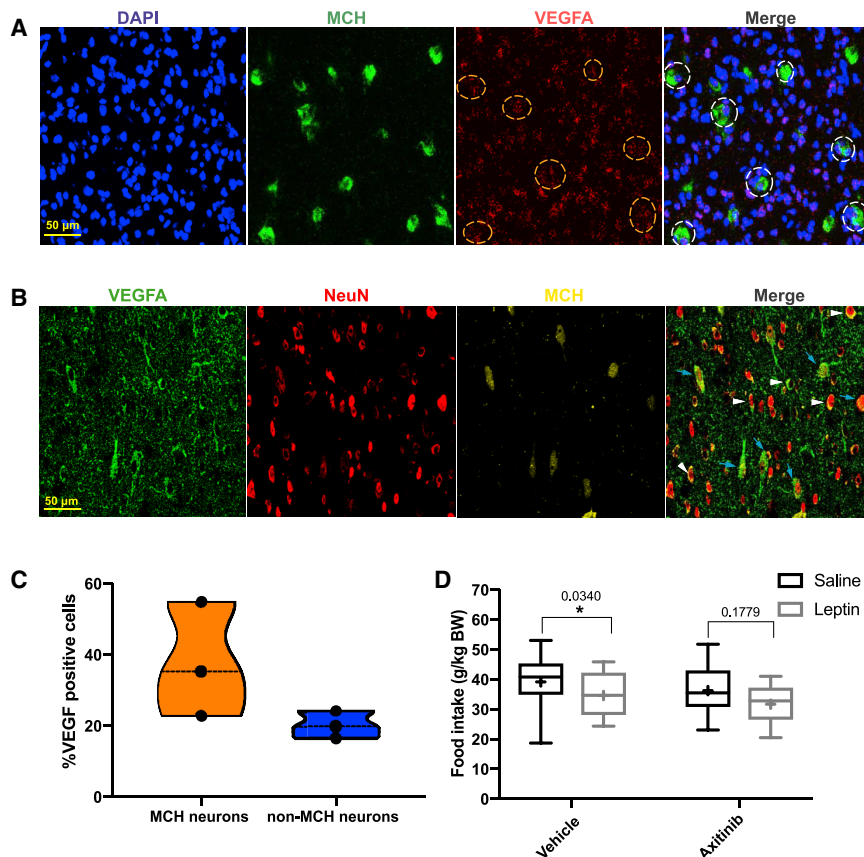
Figure 7. VEGFA Expression in MCH Neurons

(A) Representative images from *in situ* hybridizations for VEGFA and MCH in LHA sections. Green, MCH; red, VEGFA; blue, 4′,6-diamidino-2-phenylindole (DAPI). In the merged image, white dashed circles show coexpression of VEGFA and MCH. Orange dashed circles in the VEGFA expression image are corresponding positions to white dashed circles.

(B) Representative images of immunoactive VEGFA, NeuN, and MCH/tdTomato signal in LHA sections. Green, anti-VEGFA; red, anti-NeuN, neuronal marker; yellow, tdTomato. In the merged image, blue arrows point out MCH neurons expressing VEGFA, and white arrows point out non-MCH neurons expressing VEGFA.

(C) Quantification of the coexpression percentage of VEGFA expression in MCH neurons, and in non-MCH neurons.

(D) Assessment of leptin sensitivity by comparing the effect of saline or leptin injection on 1-h refeeding food intake in 16-h fasted and CNO-treated-hM3Dq^{MCH} mice (n = 10) upon vehicle or Axitinib pretreatment. Data are represented in a violon plot (C); in (D), bar graphs represent the min to max value, the mean value is marked as "+". Statistical analysis: leptin sensitivity comparison by paired Student's t test, *p < 0.05. Scale bar: 50 μm in (A) and (B).

Although most energy regulatory neurocircuits, such as melanocortin neurons in the ARC, exert their metabolism regulatory function through neuropeptide and neurotransmitter-dependent signaling in their widespread neurocircuitry in a conventional way by synaptic transmission (Betley et al., 2015; Engström Ruud et al., 2020; Fenselau et al., 2017; Steculorum et al., 2016), MCH neurons have previously been shown to exert at least part of their metabolism regulatory function through additional mechanisms. First, they densely innervate the ependymal cells of the ventricle to regulate cilia beating and CSF circulation (Conductier et al., 2013). Second, they directly project to the ventricle to release MCH into the CSF and to mediate their orexigenic effect through volume transmission (Noble et al., 2018). Our present study extends the unconventional functions of MCH neurons by demonstrating that they not only release neuropeptides and transmitters but also express considerable amounts of VEGFA, as revealed by multiple complementary approaches. Thus, we provide a model that indicates that hypothalamic neurons can modulate the vascular barrier through activity-dependent release of the angiogenic factor VEGFA. It has previously been shown that in the developing CNS, neuronal VEGF maintains neurons and endothelial cells in both paracrine and autocrine manners (Mukouyama et al., 2002; Ogunshola et al., 2002). In adult animals, hippocampal-expressing VEGF is increased during exposure to an enriched environment and upon maze exposure, contributing to the effect of environment on neurogenesis and cognition (Cao et al., 2004). In addition to a role in the CNS, it has been shown that peripheral

nerves provide a template that determines the organotypic pattern of blood vessel branching and arterial differentiation in the skin, by local secretion of VEGF (Mukouyama et al., 2002; Ogunshola et al., 2002). Importantly, a recent study revealed that cultured hippocampal neurons express VEGF endogenously and VEGF localizes in vesicles, which undergo kinesin-dependent axonal transport as well as depolarization-dependent release of VEGF (Yang et al., 2017). Thus, likely a similar mechanism operates in MCH neurons, which is in line with results of Langlet et al. (2013) that showed VEGFA-dependent control of ME barrier plasticity.

The present study through use of complementary experimental approaches revealed that activating MCH neurons can modulate the permeability of the ME barrier. Future studies will have to investigate the effects on ME barrier permeability and their physiological consequences when MCH neurons are inhibited during their states of natural activation. Similarly, further defining the role of MCH-neuron-derived VEGFA will have to use mice with cell-type-specific disruption of VEGFA in these neurons.

Although MCH neurons have been implicated in both energy homeostasis and sleep regulation, only recent studies using *in vivo* Ca^{2+} imaging have unraveled the physiological regulation of these neurons in freely behaving mice. Using fiber photometry of genetically marked MCH neurons, González et al. (2016) revealed that MCH neurons increase their activity upon novel object recognition. Moreover, single-MCH-neuron-resolution-

based Ca²⁺ imaging revealed a predominant activation of MCH neurons during REM sleep (Blanco-Centurion et al., 2019), whereas in another study, it was reported that MCH neurons exhibited a more heterogenous response dependent on sleep cycles and a majority of neurons was activated during REM sleep, but minor proportions did not respond to changes in sleep state or some even became activated upon awakening (Izawa et al., 2019). These heterogenous responses are also consistent with the molecular heterogeneity of MCH neurons revealed in our single-nuclei sequencing experiments. Unfortunately, the abovementioned studies did not investigate the regulation of MCH neuron activity across changes in nutritional state. Thus, future studies are clearly needed to investigate how MCH neurons are dynamically regulated across different nutritional states *in vivo*.

Nevertheless, modulation of BBB permeability and, specifically, leptin transport has been linked to circadian regulation and sleep. Here, leptin transport is increased toward the end of the light cycle and sleep increases BBB function during the day to support the exchange of metabolites across the BBB, consistent with the activation pattern of the majority of MCH neurons during daytime (Cuddapah et al., 2019; Pan and Kastin, 2001). Interestingly, sleep restriction, which presumably alters MCH neuron activity, has been shown to modulate BBB permeability, although to a different extent based on the protocols used (Gómez-González et al., 2013; He et al., 2014). Moreover, sleep deprivation has been linked to the development of leptin resistance in the ARC, although the potential contribution of reduced leptin transport to the CNS has not been addressed in this study (Hakim et al., 2015). Thus, future studies are clearly warranted to directly investigate the functional contribution of MCH neuron regulation in the sleep-dependent control of BBB permeability and leptin sensitivity.

Given, the wide projections of MCH neurons throughout multiple sites within the CNS, including the hippocampus, as well as the profound effects of VEGF in learning and memory, MCH-neuron-dependent VEGFA release may have further reaching implications beyond the regulation of BBB permeability and associated changes in metabolic homeostasis.

Finally, our single-nuclei sequencing experiments revealed the detection of at least four molecularly distinct clusters of hypothalamic MCH neurons. Here, cluster 0 was characterized by the highest level expression of Cartp as a well-defined feeding regulatory peptide. These data are consistent with studies in which chemogenetic activation of Cartp-expressing neurons in the LHA stimulates food intake (Farzi et al., 2018). The same cluster was characterized by the expression of genes associated with VEGFA signaling, indicating that the feeding-regulatory MCH neurons may also directly regulate BBB permeability. Clearly, future studies will have to use more detailed functional analyses to investigate the activity of these MCH neuron subtypes across different sleep cycles as well as in different nutritional states and, ultimately, define their potentially distinct physiological effector pathways.

Collectively, the results of our study assign MCH neurons a role in regulating ME permeability and to modulate gating of energy-sensing-hormones to the ARC, as exemplified for leptin. Future studies have to define whether this regulation also modulates the accessibility of the ARC for other periphery-born factors and may, thus, define a novel route for how, through manipulating MCH neurons, the altered transport of energy-state-sensing hormones to the CNS, as observed in obesity, may be overcome (El-Haschimi et al., 2000).

STAR★METHODS

Detailed methods are provided in the online version of this paper and include the following:

- KEY RESOURCES TABLE
- RESOURCE AVAILABILITY
  - Lead Contact
  - Materials Availability
  - Data and Code Availability
- EXPERIMENTAL MODEL AND SUBJECT DETAILS
  - Animals and Husbandry
  - Mouse lines
- METHOD DETAILS
  - Evans Blue diffusion assay and barrier permeability assay
  - Chemogenetic MCH neuron activation for food intake and leptin sensitivity studies *in vivo*
  - Insulin tolerance test (ITT)
  - Glucose tolerance test (GTT)
  - Stereotactic Surgery
  - *In vivo* optogenetics
  - Axitinib treatment
  - Nuclear isolation for single nucleus sequencing
  - Single nucleus sorting by flow cytometry
  - Single nucleus sequencing and analysis
  - PhosphoRiboTrap Preparation
  - RNA bulk sequence
  - Fluorescence Immunostaining
  - *In situ* hybridization
  - Imaging and quantification
  - Tanycyte primary cultures
  - Immunoblotting
  - cAMP assays
  - Isolation of hypothalamic tanycytes using Fluorescence Activated Cell Sorting
  - Quantitative RT-PCR analyses
  - Electrone Microscopy
  - Ca²⁺ imaging in ME slices *in vitro*
- QUANTIFICATION AND STATISTICAL ANALYSIS

REFERENCES

Betley, J.N., Xu, S., Cao, Z.F.H., Gong, R., Magnus, C.J., Yu, Y., and Sternson, S.M. (2015). Neurons for hunger and thirst transmit a negative-valence teaching signal. Nature *521*, 180–185.

Bittencourt, J.C. (2011). Anatomical organization of the melanin-concentrating hormone peptide family in the mammalian brain. Gen. Comp. Endocrinol. *172*, 185–197.

Blanco-Centurion, C., Luo, S., Spergel, D.J., Vidal-Ortiz, A., Oprisan, S.A., Van den Pol, A.N., Liu, M., and Shiromani, P.J. (2019). Dynamic Network Activation of Hypothalamic MCH Neurons in REM Sleep and Exploratory Behavior. J. Neurosci. *39*, 4986–4998.

Brandt, C., Nolte, H., Henschke, S., Engstrom Ruud, L., Awazawa, M., Morgan, D.A., Gabel, P., Sprenger, H.G., Hess, M.E., Gunther, S., et al. (2018). Food Perception Primes Hepatic ER Homeostasis via Melanocortin-Dependent Control of mTOR Activation. Cell *175*, 1321–1335.e1320.

Butler, A., Hoffman, P., Smibert, P., Papalexi, E., and Satija, R. (2018). Integrating Single-Cell Transcriptomic Data Across Different Conditions, Technologies, and Species. Nat Biotechnol. *36*, 411–420.

Campbell, J.N., Macosko, E.Z., Fenselau, H., Pers, T.H., Lyubetskaya, A., Tenen, D., Goldman, M., Verstegen, A.M., Resch, J.M., McCarroll, S.A., et al. (2017). A molecular census of arcuate hypothalamus and median eminence cell types. Nat. Neurosci. *20*, 484–496.

Cao, L., Jiao, X., Zuzga, D.S., Liu, Y., Fong, D.M., Young, D., and During, M.J. (2004). VEGF links hippocampal activity with neurogenesis, learning and memory. Nat. Genet. *36*, 827–835.

Ciofi, P., Garret, M., Lapirot, O., Lafon, P., Loyens, A., Prévot, V., and Levine, J.E. (2009). Brain-endocrine interactions: a microvascular route in the mediobasal hypothalamus. Endocrinology *150*, 5509–5519.

Clarke, I.J. (2015). Hypothalamus as an endocrine organ. Compr. Physiol. *5*, 217–253.

Conductier, G., Brau, F., Viola, A., Langlet, F., Ramkumar, N., Dehouck, B., Lemaire, T., Chapot, R., Lucas, L., Rovère, C., et al. (2013). Melanin-concentrating hormone regulates beat frequency of ependymal cilia and ventricular volume. Nat. Neurosci. *16*, 845–847.

Cuddapah, V.A., Zhang, S.L., and Sehgal, A. (2019). Regulation of the Blood-Brain Barrier by Circadian Rhythms and Sleep. Trends Neurosci. *42*, 500–510.

Diniz, G.B., and Bittencourt, J.C. (2017). The Melanin-Concentrating Hormone as an Integrative Peptide Driving Motivated Behaviors. Front. Syst. Neurosci. *11*, 32.

El-Haschimi, K., Pierroz, D.D., Hileman, S.M., Bjørbaek, C., and Flier, J.S. (2000). Two defects contribute to hypothalamic leptin resistance in mice with diet-induced obesity. J. Clin. Invest. *105*, 1827–1832.

Engström Ruud, L., Pereira, M.M.A., de Solis, A.J., Fenselau, H., and Brüning, J.C. (2020). NPY mediates the rapid feeding and glucose metabolism regulatory functions of AgRP neurons. Nat. Commun. *11*, 442.

Farzi, A., Lau, J., Ip, C.K., Qi, Y., Shi, Y.C., Zhang, L., Tasan, R., Sperk, G., and Herzog, H. (2018). Arcuate nucleus and lateral hypothalamic CART neurons in the mouse brain exert opposing effects on energy expenditure. eLife *7*, e36494.

Fenselau, H., Campbell, J.N., Verstegen, A.M., Madara, J.C., Xu, J., Shah, B.P., Resch, J.M., Yang, Z., Mandelblat-Cerf, Y., Livneh, Y., and Lowell, B.B. (2017). A rapidly acting glutamatergic ARC→PVH satiety circuit postsynaptically regulated by α-MSH. Nat. Neurosci. *20*, 42–51.

Gómez-González, B., Hurtado-Alvarado, G., Esqueda-León, E., Santana-Miranda, R., Rojas-Zamorano, J.A., and Velázquez-Moctezuma, J. (2013). REM sleep loss and recovery regulates blood-brain barrier function. Curr. Neurovasc. Res. *10*, 197–207.

González, J.A., Iordanidou, P., Strom, M., Adamantidis, A., and Burdakov, D. (2016). Awake dynamics and brain-wide direct inputs of hypothalamic MCH and orexin networks. Nat. Commun. *7*, 11395.

Habib, N., Avraham-Davidi, I., Basu, A., Burks, T., Shekhar, K., Hofree, M., Choudhury, S.R., Aguet, F., Gelfand, E., Ardlie, K., et al. (2017). Massively parallel single-nucleus RNA-seq with DroNc-seq. Nat. Methods *14*, 955–958.

Hakim, F., Wang, Y., Carreras, A., Hirotsu, C., Zhang, J., Peris, E., and Gozal, D. (2015). Chronic sleep fragmentation during the sleep period induces hypothalamic endoplasmic reticulum stress and PTP1b-mediated leptin resistance in male mice. Sleep (Basel) *38*, 31–40.

Hassani, O.K., Lee, M.G., and Jones, B.E. (2009). Melanin-concentrating hormone neurons discharge in a reciprocal manner to orexin neurons across the sleep-wake cycle. Proc. Natl. Acad. Sci. USA *106*, 2418–2422.

Hausen, A.C., Ruud, J., Jiang, H., Hess, S., Varbanov, H., Kloppenburg, P., and Brüning, J.C. (2016). Insulin-Dependent Activation of MCH Neurons Impairs Locomotor Activity and Insulin Sensitivity in Obesity. Cell Rep. *17*, 2512–2521.

He, J., Hsuchou, H., He, Y., Kastin, A.J., Wang, Y., and Pan, W. (2014). Sleep restriction impairs blood-brain barrier function. J. Neurosci. *34*, 14697–14706.

Huang, W., Sherman, B.T., and Lempicki, R.A. (2009a). Bioinformatics enrichment tools: paths toward the comprehensive functional analysis of large gene lists. Nucleic Acids Res. *37*, 1–13.

Huang, W., Sherman, B.T., and Lempicki, R.A. (2009b). Systematic and integrative analysis of large gene lists using DAVID bioinformatics resources. Nat. Protoc. *4*, 44–57.

Izawa, S., Chowdhury, S., Miyazaki, T., Mukai, Y., Ono, D., Inoue, R., Ohmura, Y., Mizoguchi, H., Kimura, K., Yoshioka, M., et al. (2019). REM sleep-active MCH neurons are involved in forgetting hippocampus-dependent memories. Science *365*, 1308–1313.

Kim, D., Langmead, B., and Salzberg, S.L. (2015). HISAT: a fast spliced aligner with low memory requirements. Nat. Methods *12*, 357–360.

Knight, Z.A., Tan, K., Birsoy, K., Schmidt, S., Garrison, J.L., Wysocki, R.W., Emiliano, A., Ekstrand, M.I., and Friedman, J.M. (2012). Molecular profiling of activated neurons by phosphorylated ribosome capture. Cell *151*, 1126–1137.

Komagata, N., Latifi, B., Rusterholz, T., Bassetti, C.L.A., Adamantidis, A., and Schmidt, M.H. (2019). Dynamic REM Sleep Modulation by Ambient Temperature and the Critical Role of the Melanin-Concentrating Hormone System. Curr. Biol. *29*, 1976–1987.e1974.

Konadhode, R.R., Pelluru, D., Blanco-Centurion, C., Zayachkivsky, A., Liu, M., Uhde, T., Glen, W.B., Jr., van den Pol, A.N., Mulholland, P.J., and Shiromani, P.J. (2013). Optogenetic stimulation of MCH neurons increases sleep. J. Neurosci. *33*, 10257–10263.

Kong, D., Vong, L., Parton, L.E., Ye, C., Tong, Q., Hu, X., Choi, B., Brüning, J.C., and Lowell, B.B. (2010). Glucose stimulation of hypothalamic MCH neurons involves K(ATP) channels, is modulated by UCP2, and regulates peripheral glucose homeostasis. Cell Metab. *12*, 545–552.

Langlet, F., Levin, B.E., Luquet, S., Mazzone, M., Messina, A., Dunn-Meynell, A.A., Balland, E., Lacombe, A., Mazur, D., Carmeliet, P., et al. (2013). Tanycytic VEGF-A boosts blood-hypothalamus barrier plasticity and access of metabolic signals to the arcuate nucleus in response to fasting. Cell Metab. *17*, 607–617.

Li, H., Handsaker, B., Wysoker, A., Fennell, T., Ruan, J., Homer, N., Marth, G., Abecasis, G., and Durbin, R.; 1000 Genome Project Data Processing Subgroup (2009). The Sequence Alignment/Map format and SAMtools. Bioinformatics *25*, 2078–2079.

Löhr, H., Hess, S., Pereira, M.M.A., Reinoß, P., Leibold, S., Schenkel, C., Wunderlich, C.M., Kloppenburg, P., Brüning, J.C., and Hammerschmidt, M. (2018). Diet-Induced Growth Is Regulated via Acquired Leptin Resistance and Engages a Pomc-Somatostatin-Growth Hormone Circuit. Cell Rep. *23*, 1728–1741.

Ludwig, D.S., Tritos, N.A., Mastaitis, J.W., Kulkarni, R., Kokkotou, E., Elmquist, J., Lowell, B., Flier, J.S., and Maratos-Flier, E. (2001). Melanin-concentrating hormone overexpression in transgenic mice leads to obesity and insulin resistance. J. Clin. Invest. *107*, 379–386.

Macneil, D.J. (2013). The role of melanin-concentrating hormone and its receptors in energy homeostasis. Front. Endocrinol. (Lausanne) *4*, 49.

Madisen, L., Mao, T., Koch, H., Zhuo, J.M., Berenyi, A., Fujisawa, S., Hsu, Y.W., Garcia, A.J., 3rd, Gu, X., Zanella, S., et al. (2012). A toolbox of Cre-dependent optogenetic transgenic mice for light-induced activation and silencing. Nat. Neurosci. *15*, 793–802.

Martínez, F., Cifuentes, M., Tapia, J.C., and Nualart, F. (2019). The median eminence as the hypothalamic area involved in rapid transfer of glucose to the brain: functional and cellular mechanisms. J. Mol. Med. (Berl.) *97*, 1085–1097.

Mukouyama, Y.S., Shin, D., Britsch, S., Taniguchi, M., and Anderson, D.J. (2002). Sensory nerves determine the pattern of arterial differentiation and blood vessel branching in the skin. Cell *109*, 693–705.

Mullier, A., Bouret, S.G., Prevot, V., and Dehouck, B. (2010). Differential distribution of tight junction proteins suggests a role for tanycytes in blood-hypothalamus barrier regulation in the adult mouse brain. J. Comp. Neurol. *518*, 943–962.

Noble, E.E., Hahn, J.D., Konanur, V.R., Hsu, T.M., Page, S.J., Cortella, A.M., Liu, C.M., Song, M.Y., Suarez, A.N., Szujewski, C.C., et al. (2018). Control of

Feeding Behavior by Cerebral Ventricular Volume Transmission of Melanin-Concentrating Hormone. Cell Metab. *28*, 55–68.e57.

Ogunshola, O.O., Antic, A., Donoghue, M.J., Fan, S.Y., Kim, H., Stewart, W.B., Madri, J.A., and Ment, L.R. (2002). Paracrine and autocrine functions of neuronal vascular endothelial growth factor (VEGF) in the central nervous system. J. Biol. Chem. *277*, 11410–11415.

Pan, W., and Kastin, A.J. (2001). Diurnal variation of leptin entry from blood to brain involving partial saturation of the transport system. Life Sci. *68*, 2705–2714.

Pissios, P., Trombly, D.J., Tzameli, I., and Maratos-Flier, E. (2003). Melanin-concentrating hormone receptor 1 activates extracellular signal-regulated kinase and synergizes with G(s)-coupled pathways. Endocrinology *144*, 3514–3523.

Prevot, V., Cornea, A., Mungenast, A., Smiley, G., and Ojeda, S.R. (2003). Activation of erbB-1 signaling in tanycytes of the median eminence stimulates transforming growth factor beta1 release via prostaglandin E2 production and induces cell plasticity. J. Neurosci. *23*, 10622–10632.

Prevot, V., Dehouck, B., Sharif, A., Ciofi, P., Giacobini, P., and Clasadonte, J. (2018). The Versatile Tanycyte: A Hypothalamic Integrator of Reproduction and Energy Metabolism. Endocr. Rev. *39*, 333–368.

Rossi, M., Choi, S.J., O'Shea, D., Miyoshi, T., Ghatei, M.A., and Bloom, S.R. (1997). Melanin-concentrating hormone acutely stimulates feeding, but chronic administration has no effect on body weight. Endocrinology *138*, 351–355.

Schaeffer, M., Langlet, F., Lafont, C., Molino, F., Hodson, D.J., Roux, T., Lamarque, L., Verdié, P., Bourrier, E., Dehouck, B., et al. (2013). Rapid sensing of circulating ghrelin by hypothalamic appetite-modifying neurons. Proc. Natl. Acad. Sci. USA *110*, 1512–1517.

Steculorum, S.M., Ruud, J., Karakasilioti, I., Backes, H., Engström Ruud, L., Timper, K., Hess, M.E., Tsaousidou, E., Mauer, J., Vogt, M.C., et al. (2016). AgRP Neurons Control Systemic Insulin Sensitivity via Myostatin Expression in Brown Adipose Tissue. Cell *165*, 125–138.

Timper, K., Denson, J.L., Steculorum, S.M., Heilinger, C., Engström-Ruud, L., Wunderlich, C.M., Rose-John, S., Wunderlich, F.T., and Brüning, J.C. (2017). IL-6 Improves Energy and Glucose Homeostasis in Obesity via Enhanced Central IL-6 trans-Signaling. Cell Rep. *19*, 267–280.

Trapnell, C., Williams, B.A., Pertea, G., Mortazavi, A., Kwan, G., van Baren, M.J., Salzberg, S.L., Wold, B.J., and Pachter, L. (2010). Transcript assembly and quantification by RNA-Seq reveals unannotated transcripts and isoform switching during cell differentiation. Nat. Biotechnol. *28*, 511–515.

Varela, L., and Horvath, T.L. (2012). Leptin and insulin pathways in POMC and AgRP neurons that modulate energy balance and glucose homeostasis. EMBO Rep. *13*, 1079–1086.

Yang, P., Sun, X., Kou, Z.W., Wu, K.W., Huang, Y.L., and Sun, F.Y. (2017). VEGF Axonal Transport Dependent on Kinesin-1B and Microtubules Dynamics. Front. Mol. Neurosci. *10*, 424.

Yates, A., Beal, K., Keenan, S., McLaren, W., Pignatelli, M., Ritchie, G.R., Ruffier, M., Taylor, K., Vullo, A., and Flicek, P. (2015). The Ensembl REST API: Ensembl Data for Any Language. Bioinformatics *31*, 143–145.

Yu, G., Wang, L.-G., Han, Y., and He, Q.-Y. (2012). clusterProfiler: An R Package for Comparing Biological Themes Among Gene Clusters. OMICS *16*, 284–287.

STAR★METHODS

KEY RESOURCES TABLE

REAGENT or RESOURCE	SOURCE	IDENTIFIER
Antibodies		
GFP Polyclonal	Thermo Fisher Scientific	Cat#A-6455; RRID:AB_221570
Living Colors® DsRed Polyclonal	Takara Bio	Cat#632496; RRID:AB_10013483
Anti-Vimentin	Millipore	Cat#AB5733; RRID:AB_11212377
Recombinant Anti-VEGF	Abcam	Cat#ab52917; RRID:AB_883427
Living Colors® Full-Length ZsGreen Polyclonal	Clontech	Cat#632474; RRID:AB_2491179
Phospho-STAT3 (Tyr705)	Cell Signaling	Cat#9145; RRID:AB_2491009
Goat anti-Rabbit, Alex488	Thermo Fisher Scientific	Cat#A-11008; RRID:AB_143165
Goat anti-Chicken, Alex 641	Thermo Fisher Scientific	Cat#A-21449; RRID:AB_2535866
Goat anti-Rat, Alex594	Thermo Fisher Scientific	Cat#A-11007; RRID:AB_10561522
Phospho-S6 (Ser244, Ser247)	Invitrogen	Cat#44-923G; RRID:AB_2533798
Chemicals, Peptides, and Recombinant Proteins		
Clozapine N-oxide	abcam	Cat#ab141704
Recombinant murine leptin	Peprotech	Cat#450-31
Axitinib	Sigma-Aldrich	Cat#PZ0193
Evans Blue	Sigma Aldrich	Cat#E2129
Protease inhibitor EDTA free	Roche	Cat#1183617001
RNAin	Promega	Cat#N2515
Cycloheximide	Applichem	Cat#A0879,0001
PhosSTOP	Sigma Aldrich	Cat#04906837001
Calyculin A	Cell Signaling	Cat#9902S
DHPC	Avanti	Cat#850306p
Trizol	Life Technologies	Cat#10296-010
Glycogen	Invitrogen	Cat#AM9510
Protein A Dynabeads	Invitrogen	Cat#10002D
DNase I (Rnase-free)	Invitrogen	Cat#AM2223
HEPES	Applichem	Cat#A3724,0500
MgCl$_2$	Sigma Aldrich	Cat#M9272
RNase Zap	Invitrogen	Cat#AM9780/9782
HBSS	GIBCO	Cat#14175-053
NaHCO$_3$	Carl Roth	Cat#6885.2
Glucose	Applichem	CAS#14431-43-7
KCl	Sigma Aldrich	Cat#p9541
EDTA	Sigma Aldrich	Cat#E6758
NP-40	Sigma Aldrich	CAS# 9016-45-9
Buprenorphine	Bayer	PZN 01498870
Isofluran	CP-pharma	Isofluran-1mg/ml
Tramal	Grünenthal Gmbh	Cat#95005446
Meloxicam	Boehringer Ingelheim	Metacam®, 2 mg/ml
PFA	Sigma Aldrich	CAS#30525-89-4
Sucrose	Sigma Aldrich	CAS#57-50-1
Acetone	VWR chemicals	CAS#67-64-1
Ethanol	VWR chemicals	CAS#64-17-5

(*Continued on next page*)

Continued

REAGENT or RESOURCE	SOURCE	IDENTIFIER
Methanol	VWR France	CAS#9005-64-5
DAPI	Thermo Fisher Scientific	Cat#62248
DPBS (1x)	GIBCO Life Technologies	Cat#14190-094
Dimethyl sulfoxide (DMSO)	Millipore	CAS#67-68-5
Critical Commercial Assays		
TSA Plus Fluorescence kit	Perkin Elmer	Cat#NEL741001KT
EZ PREP buffer	Sigma Aldrich	Cat#NUC-101
Fluorescence Kit v2 for RNA scope	ACD RNAScope®	Cat#323100
Rat/Mouse Ghrelin (Active) ELISA kit	Merck Millipore	Cat#EZRGRA-90K
Mouse Leptin ELISA kit	Crystal Chem	Cat#90030
Ultra Sensitive Mouse Insulin ELISA kit	Crystal Chem	Cat#90080
Mouse Corticosterone ELISA Kit	Crystal Chem	Cat#80556
Chromium Single Cell 3′ Reagent Kits v3	10x Genomics	Cat#1000092 and 1000074
VEGFA probe for RNAscope	ACD RNAScope® ISH Technology	Cat#412261-C3
MCH probe for RNAscope	ACD RNAScope® ISH Technology	Cat#478721-C1
MCHR1 probe for RNAscope	ACD RNAScope® ISH Technology	Cat#317491-C1
DARPP32 probe for RNAscope	ACD RNAScope® ISH Technology	Cat#405901-C2
Deposited Data		
RNA-Seq data	This study	GEO: GSE146019
Single-nucleus sequence	This study	GEO: GSE146020
Experimental Models: Organisms/Strains		
MCH-Cre	Kong et al., 2010	N/A
ChR2-EYFP fl/fl	Jackson Laboratory	Strain#012569
hM3Dq fl/fl	Steculorum et al., 2016	N/A
ChR2-tdTomato fl/fl	Jackson Laboratory	Strain#012567
Synaptophysin-tdTomato fl/fl	Jackson Laboratory	Strain#012570
ZsGreen fl/fl	Löhr et al., 2018	N/A
tdTomato fl/fl	Jackson Laboratory	Strain#021876
Oligonucleotides		
MCH-SF for MCH-Cre line 5′ GAA AAG ATA AGG CCT TCA AGT GCT	Eurogentec Germany	N/A
MCH-SR for MCH-Cre line 5′ GAT CTT TCT GCA GTA TCT TCC TTC	Eurogentec Germany	N/A
CRE-FR for MCH-Cre line 5′ATC GAC CGG TAA TGC AGG CAA	Eurogentec Germany	N/A
CAGS_Fow for ROSA26 flox line 5′ AAAGTCGCTCTGAGTTGTTATC	Eurogentec Germany	N/A
CAGS_ RevWT for ROSA26 flox line 5′ GATATGAAGTACTGGGCTCTT	Eurogentec Germany	N/A
CAGS_ RevCAGS for ROSA26 flox line 5′ TGTCGCAAATTAACTGTGAATC	Eurogentec Germany	N/A
Software and Algorithms		
ImageJ (Version 2.0.0-rc-43/1.50e)	https://imagej.net/Welcome	https://imagej.nih.gov/ij/download.html
GraphPad Prism (Version 8 for Mac)	https://www.graphpad.com/scientific-software/prism/	https://www.graphpad.com/scientific-software/prism/
R	The R Foundation for Statistical Computing c/o Institute for Statistics and Mathematics Wirtschaftsuniversität Wien	http://www.rproject.org

Continued

REAGENT or RESOURCE	SOURCE	IDENTIFIER
Loupe Cell Brower (Version 3.0.1)	10x Genomics	https://support.10xgenomics.com/single-cell-gene-expression/software/visualization/latest/what-is-loupe-cell-browser
Equipment		
Mono Fiberoptic Cannula	Doric Lenses Inc.	MFC_200/230-0.48_6.0mm_SM3(P)_FLT
Mono Fiberoptic Patchcord	Doric Lenses Inc.	MFP_200/230/900-0.48_0.32m_FC-CM3(P)
Fiberoptic Rotary Joint	Doric Lenses Inc.	FRJ_1x1_FC-FC
Homogenization Cylinder (borosilicate glass)	Sartorius	Cat# BBI-8542309

RESOURCE AVAILABILITY

Lead Contact
Further information and requests for resources and reagents should be directed to and will be fulfilled by the lead contact, Jens C. Brüning (bruening@sf.mpg.de).

Materials Availability
This study did not generate new unique reagents

Data and Code Availability
PhosphoRiboTrap sequencing data generated in this study are available under GEO accession "GSE146019"
   Single nucleus sequencing data generated in this study are available under GEO accession "GSE146020."

EXPERIMENTAL MODEL AND SUBJECT DETAILS

Animals and Husbandry
All animal procedures were conducted in compliance with protocols approved by the local authorities (Bezirksregierung Köln) and were in accordance with NIH guidelines. Mice were housed at 22–24°C with 12 hr light/dark cycle. Animals had *ad libitum* access to water and a standard rodent chow (ssniff V1554, 59494 Soest, Germany). Mice were housed in individually ventilated cages (IVCs). For leptin sensitivity experiments, mice were single housed and littermates of animals from the same breedings were randomly assigned to the order of experimental treatments. All studies, except the study using Synaptophysin-tdTomato[MCH] and hM3Dq[MCH] mice for electron microscopy and investigation of MCH effect on tanycyte culture signaling, which were performed in Lille, France in the laboratory of Dr. Vincent Prevot and approved by the French Ministere de l'Education Nationale, de l'Enseignement Superieur et de la Recherche (APAFIS#2617-2015110517317420 v5) and Ca^{2+} imaging experiments, which were performed at the University of Lübeck in the laboratory of Prof. Markus Schwaninger, were conducted at the Max Planck Institute for Metabolism Research, Cologne, NRW, Germany.

Mouse lines
MCH-Cre mice
This line was kindly provided by the lab of Bradford B. Lowell (Kong et al., 2010). The animals were maintained by backcrossing them on a C57BL/6N background.
hM3Dq[MCH] mice
MCH-Cre mice were mated with hM3Dq fl/fl mice, which express hM3Dq in a Cre-dependent manner from the ROSA26 locus (Steculorum et al., 2016).
ChR2-eYFP[MCH] and ChR2-tdTomato[MCH] mice
B6;129S-Gt(ROSA)26Sortm32(CAG-COP4*ChR2(H134R)EYFP) Ai32 and B6;129S-Gt(ROSA)26Sortm32(CAG-COP4*ChR2(H134R)tdTomato) Ai27 mice were obtained from Jackson laboratory (Stock number # 012569 and 012567) (Madisen et al., 2012). Homozygous ChR2-eYFP^{+/+} or ChR2-tdTomato^{+/+} mice were mated with MCH-Cre tg/wt mice to generate the ChR2-eYFP[MCH] and ChR2-tdTomato[MCH] mice.
Synaptophysin-tdTomato[MCH] mice
B6;129S-Gt(ROSA)26Sortm34.1(CAG-Syp/tdTomato)Hze/J mice were obtained from Jackson laboratory (stock number #012570) (Zeng H. 2011; Direct Data Submission 2011/04/15). The homozygous mice were mated with MCH-Cre tg/wt mice to generate Synaptophysin-tdTomato[MCH] mice.

ZsGreen^MCH mice

R26-fl-rxΔ-ZsGreen mice have been previously described (Löhr et al., 2018). Homozygous mice were mated with MCH-Cre tg/wt mice to generate ZsGreen^MCH mice.

tdTomato^MCH mice

tdTomato reporter mice were obtained from Jackon laboratory (B6;129S6-Gt(ROSA)26Sortm9(CAG-tdTomato)Hze/J) (Madisen et al., 2012). The homozygous mice were mated with MCH-Cre tg/wt mice to generate tdTomato^MCH mice.

All the mouse experiments in this study were using male mice on a C57BL/6N background (Charles River, Laboratories (Sulzfeld, Germany)) at the age of 10-16 weeks, unless otherwise mentioned.

METHOD DETAILS

Evans Blue diffusion assay and barrier permeability assay

The procedure was performed as previously described (Langlet et al., 2013; Mullier et al., 2010). hM3Dq^MCH and ChR2-tdTomato^MCH and their corresponding litter mates at the age of 15 weeks were fasted for 16 hr (from 6pm to 10am next morning). After 12 hr of fasting, mice were intraperitoneally (i.p.) injected with CNO (3mg/kgBW) or photostimulated, (3.5 hr). After 15 hr 40 min fasting time, mice were injected with sterile 1% Evans Blue dye (Sigma) in 0.9% saline by tail vein injection and sacrificed by decapitation 20 min later. Brains were acutely removed and embed in O.C.T and frozen in cold isopentane with liquid nitrogen ($-55°C$). The frozen brain were cut into 10 μm-sections and directly imaged under a fluorescence microscope. For assessment of MECA-32 and ZO-1 immunoreactivity via IHC, different cohorts of animals received the same treatment. However, the frozen brains were cut into 20 μm-sections and stored in the $-80°C$ until processing barrier immunofluorescence staining.

The protocol for barrier immunofluorescence staining has been described previously (Mullier et al., 2010), but primary antibodies used were MECA-32 (1:500, 550563, BD biosciences); ZO-1 (1:400, 61-7300, Thermo Fisher Scientific); Vimentin (1:2000, AB5733, Millipore) and secondary antibodies were goat anti-Rat Alex594 (1:500, A11007, Thermo Fisher Scientific), goat anti-Chicken Alex641 (1:500, A21449, Thermo Fisher Scientific); goat anti-Rabbit Alex488 (1:500, A11008, Thermo Fisher Scientific).

Chemogenetic MCH neuron activation for food intake and leptin sensitivity studies in vivo

hM3Dq^MCH mice and control littermates at the age of 10-13 weeks were single housed with food hoppers and handled for at least 3 days before the experiment started. At the experimental days, mice were fasted for 16 hr, and then given CNO (ab141704, abcam, dissolved in 1.5% DMSO, 3mg/kg body weight) via i.p. injection after 12 hr of fasting. At the time points of 16 hr fasting, mice were given saline or leptin injection (450-31, Peprotech, dissoved in saline, 6 mg/kg body weight) and 30 min later, mice were refed and food intake for each cage was measured at the 1 hr and 4 hr post-refeeding time. The mice treated with saline or leptin, in the following week were cross treated with leptin or saline. Saline treated food intake data were calculated for food intake comparison between genotypes. For individual animal, comparison between saline treated food intake and leptin treated food intake was calculated as a leptin sensitivity index.

Insulin tolerance test (ITT)

Insulin tolerance test was performed in 16 hr fasted mice. Mice were given i.p. CNO (3 mg/kg body weight) 4 hr before basal blood glucose level measurement. Mice were given i.p. injection with insulin (0.38 I.E./kg body weight, Lilly Deutschland GmbH, PNZ 02526396) and glucose concentrations in blood were measured after 15, 30 and 60 min employing a automatic glucose monitor (Bayer HealthCare Ascensia Contour).

Glucose tolerance test (GTT)

Glucose tolerance tests was performed as described for the ITT, but mice were given i.p. Glucose (20%, 10 ml/kg body weight) instead of insulin, and blood glucose concentration in blood were measured after 15, 30, 60 and 120 min.

Stereotactic Surgery

ChR2-tdTomato^MCH and control littermates at the age of 9 weeks were single housed in preparation for stereotactic surgeries of optogenetic fiber implantation. Animals were anesthetized with isofluran and placed into a stereotaxic apparatus. The stereotaxic coordinate was: AP -1.4 mm; DV 5.8 mm; ML 0 mm. Fiberoptic cannulas were obtained from Doric Lenses Inc (fiber core = 200 μm, NA = 0.48, length = 6mm, flat tip). Optical fiber was implanted above the median eminence at the stereotaxic coordinate described above and fixed to the skull with dental acrylic. Animals were i.p. injected with buprenorphine (PZN01498870, Bayer, 0.1 mg/kgBW) during the operation period and meloxicam (5 mg/kg bodyweight) was given subcutaneously (s.c.) for the analgesia in the first hour post-surgery and Tramadol was provided in the drinking water (1 mg/ml) twice a day during post-surgery periods for consecutive three days. Body weights were continuously monitored during recovery.

hM3Dq^MCH mice and control littermates at the age of 9 weeks underwent through same surgery for optical fiber implantation in control experiments.

After 1 week of post-surgery recovery, mice were adapted to optogenetic cages (TSE systems) or homecage with food hopper for another week and body weights were monitored every two days.

In vivo optogenetics

Fiber-implanted ChR2-tdTomato[MCH] mice and control littermates were connected to patch-cords before the experiments. Mice were fasted 16 hr (from 6pm to 10am next morning), at the time points of 12 hr fasting, mice received the light illumination (pulse duration 10 μs, frequency 10 Hz, 1 s stimulation in every 5 s, 10 mW) for three and half hr. At the 16 hr fasting time, mice were given saline or leptin (6 mg/kg body weight) i.p. injection. 30 min later, mice were refed and food intake for each cage was measured at the 1 hr and 4 hr post-refeeding time. The mice treated with saline or leptin, were cross-treated with leptin or saline in the following week. At the end of experiment, all the mice were perfused with 4% PFA, brains were post-fixed and cryoprotected in 20% sucrose. The brains were frozen and cut for fiber placement validation. Only the data with correct placement of fiber implantation was included in the analysis. Data analysis was performed as described for chemogenetic experiment.

Axitinib treatment

Male hM3Dq[MCH] mice at the age of 10-14 weeks were used for this experiment. Mice were fasted starting at 6 p.m. Axitinib (PZ0193, Sigma, 25 mg/kgBW in PEG/H2O 3:7 mixed, PH 2.5) or vehicle (PEG/H$_2$O 3:7 mixed, PH 2.5) were injected i.p. at 5 a.m. (after 11 hr of fasting), CNO (3 mg/kgBW) was injected to all mice at 6 a.m. (after 12 hr of fasting). Leptin (6 mg/kgBW) or saline were injected i.p. at 10 a.m. (after 16 hr of fasting). 30 min after leptin/saline injection, mice were refed and food intake was monitored 1 hr and 4 hr after refeeding. In the following three weeks, mice were given cross-over injections with either vehicle/axitinib or saline/leptin.

Nuclear isolation for single nucleus sequencing

The nuclear isolation method was modified from Habib et al. (2017). Hypothalami of ZsGreen[MCH] mice were dissected and collected into 1ml of ice-cold EZ PREP buffer (D8938, Sigma). The tissue was homogenized with a glass dounce, twice at 250 rpm and 12 times at 1000 rpm and incubated on ice for 5 min. Nuclei were centrifuged at 500 g, 5 min after addition of 4 mL of nuclear lysis buffer and incubated on ice for 5 min. The supernatant was discarded and the pellet was resuspended in 4 mL nucleus suspension buffer (NSB, 1x PBS, 0.01% BSA, and 0.1% RNase inhibitor (352235, Clontech). Nuclei were centrifuged at 500 g for 2 min. The supernatant was discarded and isolated nuclei were resuspended in 300 μl NSB and then filtered through a 30 μm cell strainer into sorting tubes for flow cytometry sorting on a BD FACSAria IIIu.

Single nucleus sorting by flow cytometry

Nuclei suspension from ZsGreen[MCH] mice was stained with DAPI (1:1000, 62248, Thermo Fisher Scientific) as nuclear marker. ZsGreen positive nuclei + DAPI positive nuclei were collected as MCH neuron nuclei. A FACSAria IIIu was used for gating and sorting nuclei. Single nuclei were identified based on side scatter (SSC-A) and DAPI fluorescence (area versus width). ZsGreen fluorescence was detected with 488 nm excitation and 530 nm emission. Sorting was performed at 4°C with a 70 μm nozzle. Sorted ZsGreen positive nuclei were collected into 1xPBS buffer with 0.04% BSA for 10x genomics single cell sequencing.

Single nucleus sequencing and analysis

For snRNA library construction, Chromium Single Cell 3′ Reagent Kits v3 were used. The Single Cell 3′ Protocol upgrades short read sequencers to deliver a scalable microfluidic platform for 3′ digital gene expression profiling of up to 10,000 individual nuclei per sample. The 10x GemCode Technology samples a pool of ~750,000 barcodes to separately index each cell's transcriptome. It does so by partitioning thousands of cells into nanoliter-scale Gel Bead-In-EMulsions (GEMs), where all generated cDNA share a common 10x Barcode. Libraries were generated and sequenced from the cDNA and the 10x Barcodes were used to associate individual reads back to the individual partitions.

Single nucleus suspensions in 1xPBS containing 0.04% BSA (700-1200 nuclei/μl) were checked for viability which should ideally exceed 75% and be free of debris and cell aggregates. To achieve single cell resolution, the cells were delivered at a limiting dilution, such that the majority (~90- 99%) of generated GEMs contains no cell, while the remainder largely contain a single cell. Upon dissolution of the Single Cell 3′ Gel Bead in a GEM, primers containing (i) an Illumina R1 sequence (read 1 sequencing primer), (ii) a 16 bp 10x Barcode, (iii) a 12 bp Unique Molecular Identifier (UMI) and (iv) a poly-dT primer sequence were released and mixed with cell lysate and Master Mix. Incubation of the GEMs produced barcoded, full-length cDNA from poly-adenylated mRNA. After incubation, the GEMs were broken and the pooled fractions were recovered. Silane magnetic beads were used to remove leftover biochemical reagents and primers from the post GEM reaction mixture. Full-length, barcoded cDNA was amplified by PCR to generate sufficient mass for library construction. Enzymatic fragmentation and size selection were used to optimize the cDNA amplicon size prior to library construction. R1 (read 1 primer sequence) were added to the molecules during GEM incubation. P5, P7, a sample index and R2 (read 2 primer sequence) were added during library construction via End Repair, A-tailing, Adaptor Ligation and PCR. The final libraries contained the P5 and P7 primers used in Illumina bridge amplification. A Single Cell 3′ Library comprised standard Illumina paired-end constructs which begin and end with P5 and P7. We allocated Illumina NovaSeq6000 S2 flowcells to sequence with the first read 28nt (cell specific barcode and UMI) and generated with the second read 90nt 3′mRNA transcriptome data. Using the v3 version of chemistry, 25k reads/nucleus were sufficient to allow comprehensive snRNA analysis.

PhosphoRiboTrap Preparation

Mice were sacrificed by decapitation. Hypothalamus sections were rapidly dissected in ice-cold 1xHBSS using a stainless brain matrix (World Precision Instruments). Arcuate nucleus and ME regions were collected into EP tubes and acutely frozen on liquid nitrogen. Collected tissues were stored at −80°C until further use.

Samples were transferred to a homogenization cylinder (Sartorius) with 1ml homogenization buffer (10 mM HEPES, 150 mM KCl, 5 mM MgCl$_2$, 2.5 mM DTT, 1/4 tablet/ml Protease inhibitors (EDTA free), 100 units/ml RNAsin, 250 μg/ml Cycloheximide, 1 tablet/ 10 mL PhosSTOP, 100 nM Calyculin A). Samples were homogenized 2 times at 250 rpm, and 9 times at 750 rpm. Homogenates were transferred to Eppendorf tubes and clarified at 2,000 g for 10 min, at 4°C. Supernatants were transferred to a new EP tube on ice and 70 μL of 10% NP40 (Sigma Aldrich) and 70 μL of 1,2-dihexanoyl-sn-glycero-3-phosphocholine (DHPC, Avanti) were added. This solution was mixed by inversion, incubated on ice for 2 min and clarified by centrifugation at 17,000 g for 10 min at 4°C. The harvested supernatant was transferred to a new EP tube, 50 μL was removed to another new EP tube, 950 μL Trizol and 50 μL glycogen (5 mg/ml) were added. This sample was incubated on ice as input. 20 μL pphospho-S6 244/247 antibody (44-923G, Invitrogen) were added to the remaining harvested supernatant and mixed well. Sample-antibody solution was incubated on ice for 1.5 hr at 4°C with gentle rotation. 100 μL Protein A Dynabeads per sample was washed 3 times with washing buffer 0.15 M (10 mM HEPES, 150 mM KCl, 5 mM MgCl$_2$, 1% NP40). The "sample-antibody" was added into the beads and incubated for 1 hr, at 4°C with gentle rotation. Sample-antibody solution was quick spinned for 2 s and placed on the cold magnet for washing 4 times with washing buffer 0.35 M (10 mM HEPES, 350 mM KCl, 5 mM MgCl$_2$, 1% NP40, 1.25 mM DTT, 100 units/ml RNAsin, 125 μg/ml Cycloheximide, 50nM Calyculin A). Beads were collected by magnetic absorption. After the last wash, the supernatant was removed and 1 mL Trizol was added to the beads and gently resuspended by pipetting and incubated on ice for 5 min. Input and IP RNA were isolated and purified by the following steps. 200 μL CHCl$_3$ was added to the samples, vortexed thoroughly and incubated in room temperature for 5 min. The samples were centrifuged at 12,200 g for 10 min at 4°C. The aqueous phase was collected and added to 550 μL of ice cold isopropanol and incubated on ice for 15 min for RNA precipitation. The samples were centrifuged at speed of 12,200 g for 15 min at 4°C. The precipitated RNA was washed by adding 1 mL of ice cold 80% ethanol and centrifuged at speed of 7,500 g for 15 min at 4°C. Ethanol was discarded and the RNA was DNaseI digested (30 μL nuclease free water dissolved-RNA pellet, 3.7 μL DNase 10X buffer, 2 μL RNAsin inhibitor and 2 μL DNaseI) for 30 min at 37°C. DNaseI was deactivated by thorough vortexing. RNA concentrations were assessed employing the Invitrogen Qbit System and were stored in −80°C until being sent for RNA bulk sequencing.

RNA bulk sequence

Pre-amplification using the Ovation RNASeq System V2 was performed. Total RNA was used for first strand cDNA synthesis, using both poly(T) and random primers, followed by second strand synthesis and isothermal strand-displacement amplification. For library preparation, the Illumina Nextera XT DNA sample preparation protocol was used, with 1 ng cDNA input. After validation (Agilent 2200 TapeStation) and quantification (Invitrogen Qubit System) all 24 transcriptome libraries were pooled. The pool was quantified using the Peqlab KAPA Library Quantification Kit and the Applied Biosystems 7900HT Sequence Detection and sequenced on a Illumna NovaSeq S2 flowcell with a PE100 protocol. The RNA sequencing pipeline utilizes the GRCm38 assembly of the mouse genome as gene sets from Ensembl release 96 (Yates et al., 2015). We quantified the gene expression of each sample by (1) aligning the RNA-sequencing reads to the mm10 reference genome using hisat 2.1.0 (Kim et al., 2015). (2) computationally depleted rRNA reads using samtools 1.8.0 (Li et al., 2009) and (3) transcript assembly and quantification as well as differential analysis between the experimental conditions using the cufflinks 2.2.1 suite (Trapnell et al., 2010). Genes are denoted as statistically significant using the standard cuffdiff cutoff (q ≤ 0.05). The Gene Ontology (GO) (Trapnell et al., 2010) term analysis based on the differentially expressed genes was carried out using Huang et al. (2009a, 2009b).

Fluorescence Immunostaining

Adult mice from ChR2-eYFP[MCH] and Synaptophysin-tdTomato[MCH] lines were perfused with 4% PFA in PBS. Brains were postfixed with 4% PFA for 4 hr and incubated in 20% sucrose in PBS overnight for cryoprotection. Frozen brains were cut on a cryostat and the sections were kept in anti-frozen medium. The floating sections were stained with GFP antibody (A6455, Thermo Fisher Scientific, 1:1000, Rabbit) for ChR2-eYFP[MCH] mice and DsRed (632496, Clontech, 1:1000, Rabbit) for Synaptophysin-tdTomato[MCH] mice. Brains were co-stained with anti-Vimentin (AB5733, Merck Millipore, 1:2000, Chicken) and DAPI (62248, Thermo Fisher Scientific, 1:1000). Staining procedure was performed as previously described (Hausen et al., 2016). Secondary antibodies: goat anti-Rabbit, Alex488 (A11008, Thermo Fisher Scientific); goat anti-Chicken, Alex 641 (A21449, Thermo Fisher Scientific). For pStat3 analysis, hM3Dq[MCH] mice and control litter mates at the age of 10-13 weeks were treated with leptin treatment for 45 min. Mice were perfused with 2% PFA in PBS. Removed brains were postfixed with 2% PFA for 2 hr and incubated in 20% sucrose in PBS overnight for cryoprotection. Every fourth section throughout the Arc was processed for pSTAT3 staining. Immunostaining procedure and pSTAT3 antibody were performed as previously described (Timper et al., 2017).

For alternative assessment of leptin signaling, hM3Dq[MCH] mice and control littermates at the age of 10-13 weeks were treated with leptin for 15 min. Mice were decapitated acutely 15 min after leptin injection. Brains were acutely removed and embed in O.C.T and frozen in cold isopentane with liquid nitrogen (−55°C). The frozen brain were cut into 20 μm-sections. Sections were fixed in 2% PF (paraformaldehyde) made in Phosphate Buffer, pH = 7.4 for 45-60 min and then rinsed in 0.02 M KPBS. Pretreatment

of sections in 0.5% NaOH + 0.5% H_2O_2 (in 0.02M KPBS) for 20 min at room temperature, then sections were rinsed in 0.02 M KPBS for 5 min, 5 times. 0.3% Glycine (in 0.02M KPBS) for 10 min at room temperature, Then were rinsed again in 0.02M KPBS for 5 min, 5 times. After that, sections were rinsed with 0.03% SDS (in 0.02M KPBS) for 10 min at room temperature and then rinsed in 0.02M KPBS for 5 min, 5 times. Sections were incubated in blocking solution (4% Normal Goat Serum (NGS) + 0.3% Triton X-100 in 0.02M KPBS) for 30 min at room temperature. After blocking, primary antibody: Rabbit anti-pSTAT3 (Tyr 705) (Cell Signaling Ref# 9131) was diluted respectively at 1:1000 in blocking solution and incubated sections for 48 hr at 4°C. Samples were rinsed with 0.02M KPBS for 5 min, 5 times and samples were incubated with secondary antibody (goat anti-Rabbit Alexa-568 and goat anti-Rat Alex-488) diluted at 1:500 in blocking solution for 2 hr at room temperature. Samples were rinsed again afterward with 0.02M KPBS for 5 min, 5 times and counterstained with Hoechst (1:10000 in 0.02M KPBS) for 3 min at room temperature and rinsed again and covered with coverslip slightly. Samples were kept at 4°C until imaging.

tdTomato[MCH] reporter mice were perfused and stained similar to ChR2-eYFP[MCH-Cre] and Synaptophysin-tdTomato[MCH], but primary antibodies used were NeuN (ABN91, Merck Millipore) and VEGF antibody (ab52917, Abcam).

In situ hybridization

Fluorescence *in situ* hybridization for simultanous detection of tdTomato and VEGFA, MCHR1 and DARPP32 was performed using RNAscope assays as previously described (Brandt et al., 2018). The tdTomato probe constitutes 20 oligo pairs, and targeted region 7-1382 (317041-C2, ACD RNAscope®), the VEGFA probe constitutes 20 oligo pairs and target region 946-2156 (Acc. No: NM_001025257.3, 412261-C3, ACD RNAscope®), The MCHR1 probe constitutes 20 oligo pairs, and targeted region 924-2145 (317491-C1, ACD RNAscope®). DARPP32 consititutes 20 oligo pairs and targeted regions 590-1674 (405901-C2, ACD RNAscope®).

Imaging and quantification

Images were captured using a confocal Leica TCS SP-8-X microscope Tile scans and Z stacks with optical section-1.0 μm were obtained for the whole ARC and Median Eminence region

For quantification of Evans blue diffusion, the Evans Blue signal was directly visualized and imaged using a 10x objective in the defined region of interest in the ARC. Images from 16 sections of 10 μm thickness per bilateral ARC per animal were taken. The defined area of ~340,000 μm^2 under identical imaging settings were isolated from the whole images and the mean gray values were calculated. The averaged value of total gray values from 16 sections per ARC per animal is the value as representative of one animal. For the comparison, the normalized gray value of each animal was normalized to the mean averaged gray value of control animals.

Quantitative analysis for tight junction organization and fenestrated capillary loops was performed as previously described (Langlet et al., 2013). The whole ARC was classified in 4 different zones (see Figure S1). For fenestrated capillary loops, ARC regions from 20 μm sections were imaged under 20x glycerol lens and Z stacks with optical section-1.0 μm for quantification. MECA-32-immunoreactive vessels were visualized in zone 2, zone 3 and zone 4. The total number from zone 2 and zone 3 from 8 sections per ARC per animal were evaluated for statistical comparison. For tight junction organization, ZO-1 staining from 20 μm sections was imaged under 40x oil lens and Z stacks with optical section-1.0 μm for quantification. The ARC and Median Eminence were separately captured without tile scan. The pixel values from 8 sections in zone 2 and zone 3 per ARC per animals were averaged as a representative of one animal.

pSTAT3 positive cells were visualized in the ARC. The number of pSTAT3-positive cells in four different zones in the ARC were manually counted using ImageJ. The total number of ARC represent the sum of the average number of positive cells for sections in zone1-4 with 2-6 sections averaged per zone.

Tanycyte primary cultures

Tanycytes were isolated from tissue explants containing the median eminence and the wall of the third ventricle from 10-day-old Sprague Dawley rats (Janvier, France) as described previously (Prevot et al., 2003). Briefly, tissue chunks were collected in culture medium (DMEM high-glucose medium containing 10% fetal calf serum, 1% penicillin/streptomycin, and 2 mM L-glutamine, Thermo Fisher) on ice and were scraped through a nylon mesh (20 μm, Merck Millipore), centrifuged and resuspended in fresh culture medium. Dissociated cells were plated in 75 cm^2 culture flasks and maintained under humid atmosphere of 5% CO_2-95% air at 37°C. Culture medium was first changed after 10 days and subsequently every 2-3 days. When cultures reached confluency, cells were passaged using trypsin/EDTA digestion and plated in 6-well plates for experiments. At 70% of confluency, tanycytes were placed into serum-free medium (DMEM/F12 without phenol red, 1% penicillin/streptomycin and 2 mM L-glutamine, all from Thermo Fisher) containing 5 ug/mL insulin (Sigma-Aldrich, USA) and 100 μM putrescine (Sigma-Aldrich, USA) for 2 days. One hour before the experiment started, cells were placed in fresh serum-free medium and treated with MCH 1 μM (Bachem, ref: H-1482) or PBS. After treatment, cells were briefly washed in ice-cold PBS and snap-frozen on dry ice.

Immunoblotting

Cells were lysed in 100 μL in freshly prepared lysis buffer (pH 7.4, 25 mM Tris, 50mM β-glycerophosphate, 1.5 mM EGTA, 0.5 mM EDTA, 1 mM sodium pyrophosphate, 1 mM sodium orthovanadate, 10 mg/ml leupeptin and pepstatin, 10 mg/ml aprotinin, 100 mg/ml

phenylmethyl sulfonyl fluoride and 1% Triton X-100). The cells lysates were cleared by centrifugation at 12,000 g for 15 min and protein content was determined using the Bradford method (BioRad, Hercules, CA). We added 4x sample buffer (Invitrogen) and 10x reducing agent (Invitrogen) to the samples and boiled them for 5 min before electrophoresis at 150V for 60 min in precast 3%–8% SDS–polyacrylamide Tris-acetate gels according to the protocol supplied with the NuPAGE system (Invitrogen, Carlsbald, CA). When necessary, the samples were stored at –80°C until use. After size-fractionation, the proteins were transferred onto Nitrocellulose membranes (0.2 mm pore-size membranes; LC2002; Invitrogen) in the blot module of the NuPAGE system (Invitrogen) for 75 min in ice. Membranes were blocked for 1 hr in TBS with 0.05% Tween 20 (TBST) and 5% non-fat milk at room temperature, incubated overnight at 4°C with their respective primary antibodies and washed four times with TBST before being exposed to horseradish peroxidase-conjugated secondary antibodies diluted in 5% non-fat milk-TBST for 1 hr at room temperature. The immunoreactions were detected with enhanced chemiluminescence (NEL101, PerkinElmer, Boston, MA). The mouse monoclonal anti-actin (A5441 Sigma; 1:5,000), rabbit monoclonal anti-phospho-AKT (Ser473; 4060 Cell Signaling; 1:1,000), rabbit monoclonal anti-AKT (4691 Cell Signaling; 1:1,000), rabbit polyclonal anti-phospho- p44/42 MAPK (p-Erk1/2) (9101 Cell Signaling; 1:1,000), rabbit polyclonal anti-p44/42 MAPK (Erk1/2) (9102 Cell Signaling; 1:1,000) were used. Secondary antibodies used for western blotting detection (anti-mouse (1:2,000) and anti-rabbit (1:2,000), all horseradish peroxidase-conjugated) were purchased from Sigma and Vector Laboratories.

cAMP assays
Primary tanycytes were seeded in 12 wells plates; at 70% confluency, cells were placed into serum-free medium (DMEM/F12 without phenol red, 1% penicillin/streptomycin and 2 mM L-glutamine, all from Thermo Fisher) and 5ug/mL insulin and 100 μM putrescine (last two from Sigma-Aldrich, USA)) for 2 additional days. 1 hr before the experiment, cells were placed into fresh serum-free medium and treated with MCH 1 μM (Bachem, H-1482), 0, 15, 30, 60 min in the presence or absence of Forskolin 10 μM (Cell Signaling, 3828), which was added 15 min before stopping treatment. At the end of the treatment, cells were washed 3 times with ice-cold PBS and 600 μL of 1x lysis buffer was added to each well. Then, cAMP levels were assessed following the instructions of the kit's datasheet (Cell signaling, 4339).

Isolation of hypothalamic tanycytes using Fluorescence Activated Cell Sorting
Median eminences from tat-cre-injected tdTomato$^{loxP/loxP}$ mice fed *ad libitum* (n = 8), were microdissected, and enzymatically dissociated using Papain Dissociation System (Worthington, Lakewood, NJ) to obtain single-cell suspensions as described previously (Langlet et al., 2013). FACS was performed using an EPICS ALTRA Cell Sorter Cytometer device (Beckman Coulter, Inc.). The sort decision was based on measurements of tdTomato fluorescence (excitation: 488nm; detection: bandpass 675 ± 20nm) by comparing cell suspensions from tdTomato positive and wild-type animals. For each animal, around 5000 tdTomato positive cells were sorted directly into 10 μL extraction buffer: 0.1% Triton® X-100 (Sigma-Aldrich) and 0.4 U/μl RNaseOUT^{TM} (Life Technologies).

Quantitative RT-PCR analyses
For gene expression analyses, mRNAs obtained from FACS-sorted cells were reverse transcribed using SuperScript® III Reverse transcriptase (Life technologies) and a linear preamplification step was performed using the TaqMan® PreAmp Master Mix Kit protocol (P/N 4366128, Applied Biosystems). Real-time PCR was carried out on Applied Biosystems 7900HT Fast Real-Time PCR System using exon-boundary-specific TaqMan® Gene Expression Assays (Applied Biosystems): Mchr1 (Mchr1-Mm00653044_m1) and Control housekeeping genes: r18S (rn18S-Mm03928990_g1); ACTB (Actb-Mm00607939_s1). Gene expression data were analyzed using SDS 2.4.1 and Data Assist 3.0.1 software (Applied Biosystem).

Electrone Microscopy
To visualize MCH nerve terminals in the median eminence at the ultrastructural level, we used a preembedding immunogold procedure. Briefly, brains of Synaptophysin-tdTomato^{MCH} mice were perfusion-fixed with 2% paraformaldehyde, 0.2% picric acid, 0.25% glutaraldehyde in 0.1 M phosphate buffer at room temperature and post-fixed overnight at 4°C. Brains were then, cut into on 80 μm thick coronal sections on a vibratome in 0.1 M PBS. Brain sections underwent aldehyde inactivation in sodium tetrahydroborate (0.1% in PBS) for 15 min, followed by permeabilization with Triton X-100 (30 min, 0.05% in 0.1 M PBS). The tissue was incubated for 40 min in a blocking solution containing 1% of BSA and 1% of normal goat serum before overnight incubation at 4°C in rabbit anti-DsRed antibodiy (632496, Clontech, 1:500, Rabbit) in incubation buffer (Triton 0.01%, BSA 0.1% and normal goat serum in PBS). Sections were then incubatred with ultra-small gold conjugate of F(ab')2 goat anti-rabbit (1:50, Aurion, 800.166) 2.5 hr at room temperature and post-fixed with 2% of glutaraldehyde 30 min at room temperature. Sections were then washed in Aurion enhancement conditioning solution (500.055). Silver enhancement was performed using Aurion silver enhancement reagents (Aurion R-Gent SE. EM, 500.033) 1 hr at room temperature and sections were postfixed with 0.5% OsO$_4$ in phosphate buffer for 15 min at room temperature.

   To determine the effect of the activation of MCH neurons on the fenestration of the ME capillary loops running along the wall of the third ventricle and reaching the ventromedial ARC, CNO-treated hM3Dq^{WT} and hM3Dq^{MCH} mice were killed by decapitation and tissue fragments containing ME and ARC microdissected under a stereomicroscope and immersion-fixed for 1 hr in 2%

paraformaldehyde, 0.2% picric acid, 1% glutaraldehyde in 0.1 M phosphate buffer at room temperature and post-fixed overnight at 4°C. After rinses in 0.1 M phosphate buffer, tissue fragments were postfixed with 1% OsO_4 for 1 hr at room temperature.

Tissues were then dehydrated through a graded series of ethanol and propylene oxide and embedded in Araldite. Semithin sections (1–2 μm thickness) were used to progressively approach the ME and ultrathin sections (80–90 nm thickness) of the region of interest were collected on Parlodion 0.8%/isoamyl acetate-coated 100 mesh grids (EMS, Fort Washington, PA). The sections were then counterstained with uranyl acetate and lead citrate before observation. Ultrathin immunolabelled sections were observed using a Zeiss transmission electron microscope 902 (Restec, Zaventem, Belgium) and images were acquired using a Gatan Orius SC1000 CCD camera (Gatan France, Grandchamp, France) at a magnifications of 7,000 x and 20,000x. All ultrastructural analyses were performed in Zone 3 (Bregma −1.82 mm; Figure S1).

Ca²⁺ imaging in ME slices *in vitro*

To measure $[Ca^{2+}]_i$ in response to ATP, MCH, glutamate and baclofen stimulation in tanycytes, acute brain slices were loaded with Fura-2 AM. Slices were incubated with Fura-2 AM (12.5 μg/ml with 0.5% DMSO and 0.05% pluronic 127, Invitrogen) in low glucose aCSF for 30 min at 37°C. Then, they were incubated in aCSF containing probenecid (1.25 mM, 30 min 37°C) and stored at 4°C before measurement.

$[Ca^{2+}]_i$ was measured using a high-speed calcium imaging setup (Till Photonics) mounted on the Axio Examiner D1 upright fluorescent microscope (Zeiss) coupled to the polychrome V monochromator and a high-speed CCD camera (Retiga EXi-blue, QImaging). Data acquisition and quantification were done using life acquisition and offline analysis software (FEI GmbH Munich, formerly Till Photonics). Brain slices were placed in a flow chamber. For the ratiometric measurement of Fura-2 we used excitation wavelengths 340 and 380 nm. Changes in the fluorescence ratio of F_{340}/F_{380} (ΔF) were normalized to basal mean values of the first 30 s (F_0) of each ROI and were shown as (ΔF/F_0).

After 1 hr of recovery in the measurement buffer (ACSF; CO_2, 5%; O_2, 95%; pH, 7.4; flow rate, 2 ml/min) stimuli, ATP, glutamate, baclofen and phaclofen were applied via the bathing medium. MCH was administered directly to the brain slice with a patch pipette. The patch pipette was placed in the lumen of the 3ʳᵈ ventricle. One min after starting the measurement, MCH (H-1482 from Bachem, 1 mM, 2 μl over 30 s), glutamate (G1626 SIGMA, 100uM), baclofen (0417, Tocris), and ATP (1 mM, 2 μl over 30 s through a glass pipette; or 100 μM during 30 s in the perfusion medium) or ACSF (2 μl over 30 s) were administered to the slice.

QUANTIFICATION AND STATISTICAL ANALYSIS

For qualitative experiments (i.e., Figures 1 and 7), representative images from 3-5 independent reporter mice are shown.

For quantitative analyses, littermates were analyzed. Similar data were obtained in at least two independent cohorts, and the pooled results for the animal numbers indicated in the figure legends are displayed.

All data from animals, which underwent *in vivo* experiments were collected and included into analysis without any outlier exclusions. Only in optogenetic experiments (Figures 5E, 5F, S5B, S5E, and S5F), data of animals with histologically verified correct fiber placement were included into the analysis. Experiments were performed in non-blinded manner except assessment of circulating hormones (Insulin, Leptin, Ghrelin, and Corticosterone) and insulin and glucose tolerance tests, which were performed in a blinded manner. For paired comparison experiments (i.e., leptin sensitivity and axitinib treatment), animals were randomly assigned among genotypes and treatments in a cross-over design and animals were allowed to recover at least for a week until next treatment.

Data presentation with bar graph was expressed as min to max value and mean value marked as "+" except Figure S6A, which is expressed as mean ± SEM. Data presentation with statistical analysis were conducted using GraphPad Prism (version 8.0). All the data for genotype comparison were analyzed using unpaired, two-tailed Student's t test, except the leptin sensitivity comparison, where a paired, two-tailed Student's t test was employed. The data to compare between both groups and genes, or both groups and time points, Two-way ANOVA was used for statistics. All p values below to 0.05 were considered significant. $*p \leq 0.05$, $**p \leq 0.01$, and $***p \leq 0.001$, $**** p \leq 0.0001$.

Supplemental Information

MCH Neurons Regulate Permeability

of the Median Eminence Barrier

Hong Jiang, Sarah Gallet, Paul Klemm, Pia Scholl, Kat Folz-Donahue, Janine Altmüller, Jens Alber, Christian Heilinger, Christian Kukat, Anne Loyens, Helge Müller-Fielitz, Sivaraj Sundaram, Markus Schwaninger, Vincent Prevot, and Jens C. Brüning
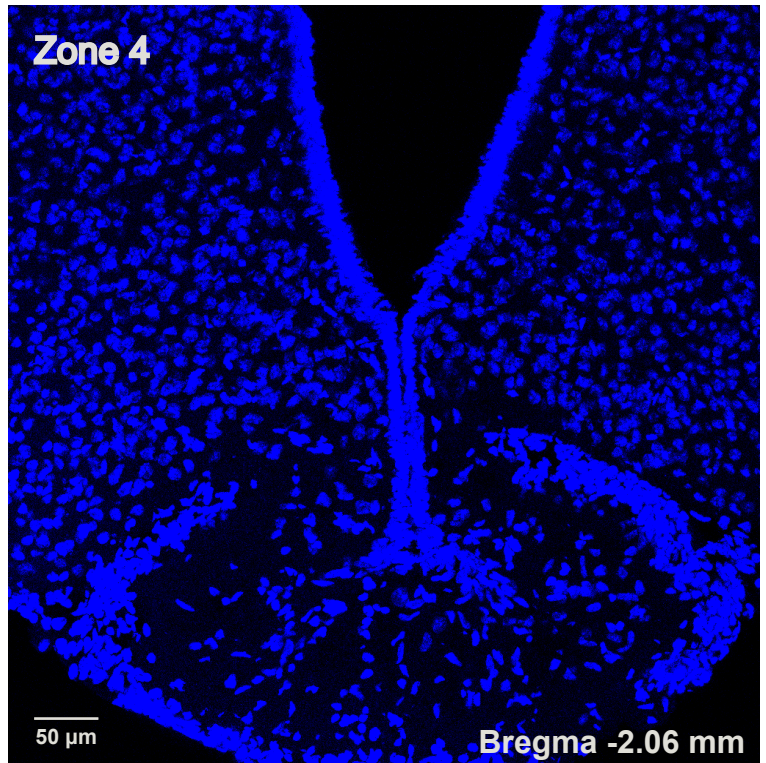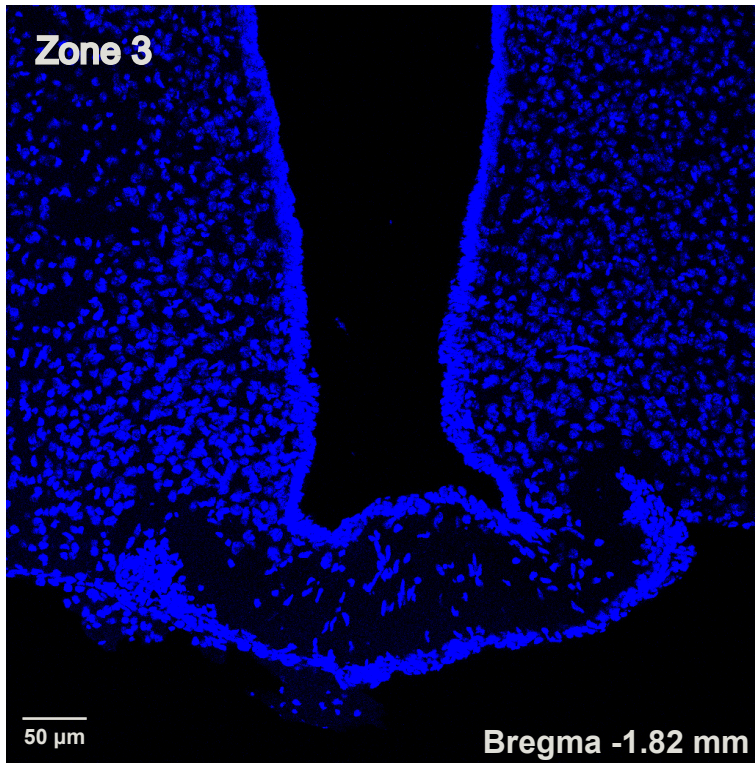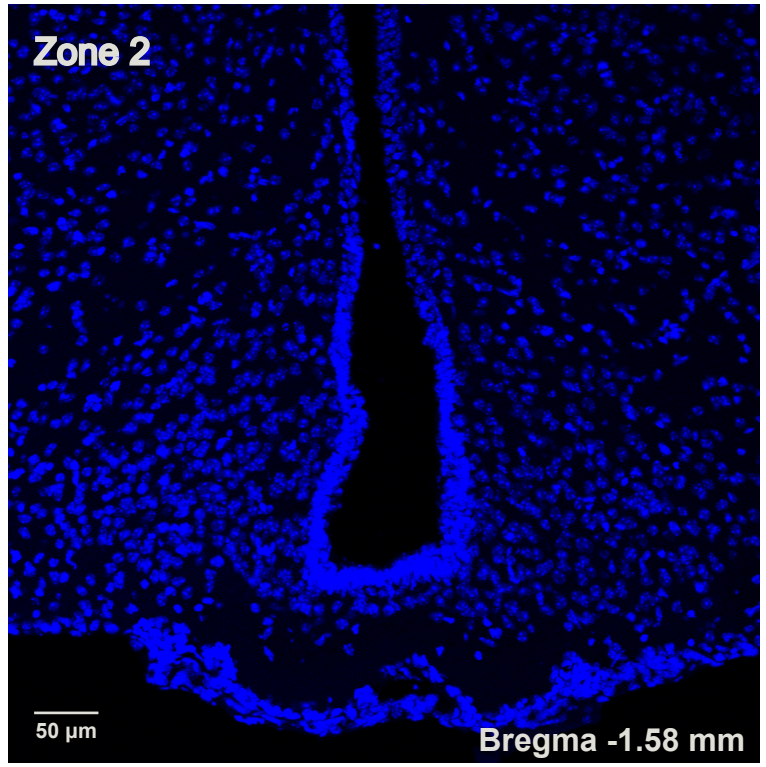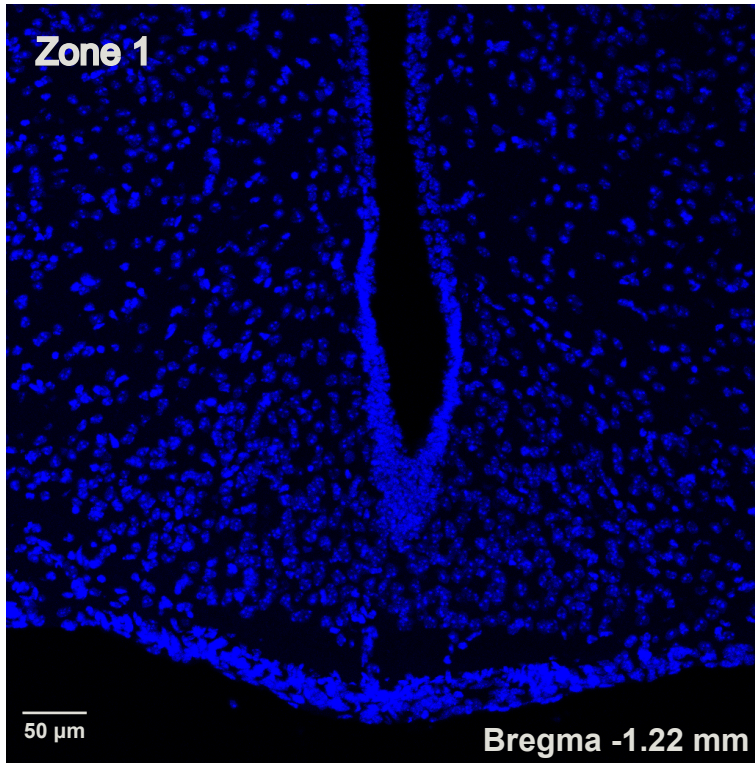
Figure S1. Related to Figure 1. Classification of four zones in the ARC. Representative anatomical location for each zone of the ARC from rostral to caudal. Scale bar: 50 µm.
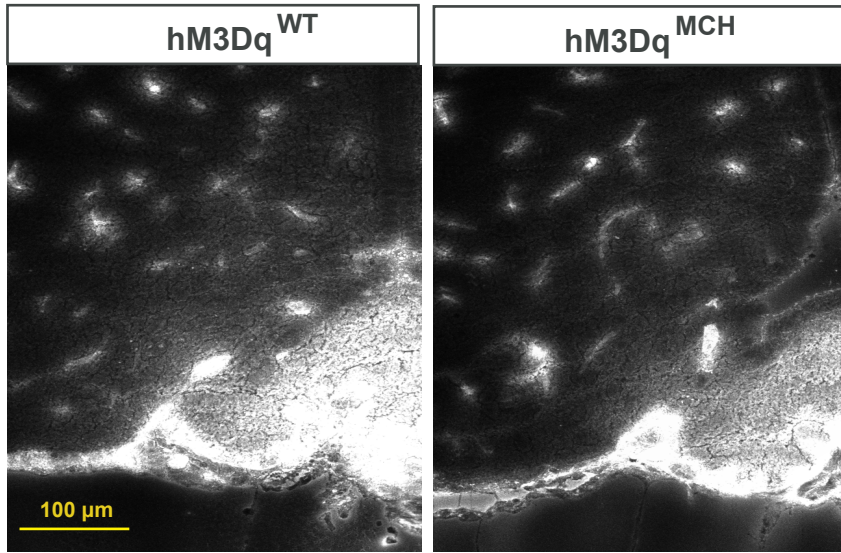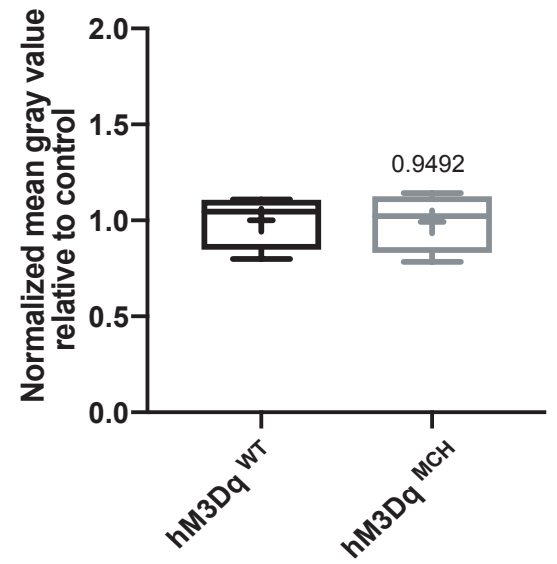
Figure S2. Related to Figure 2. Evans blue diffusion showed no detectable difference in vehicle-treated mice. (A) Representative images of Evans blue dye diffusion into the ARC region of fasted and 4 hrs vehicle-injected control and hM3Dq^{MCH} mice. (B) Quantification of Evans blue dye diffusion in the ARC region in vehicle-treated control (n=4) and hM3Dq^{MCH} (n=4) mice. Statistics: unpaired Student's T-test.
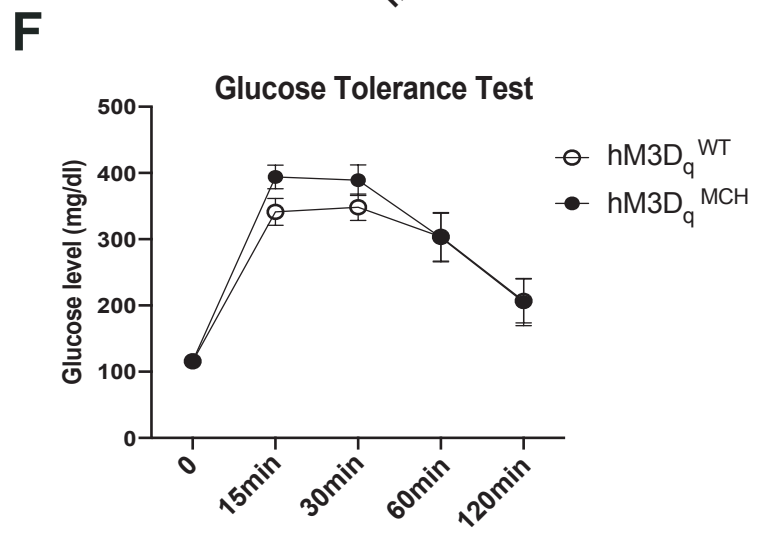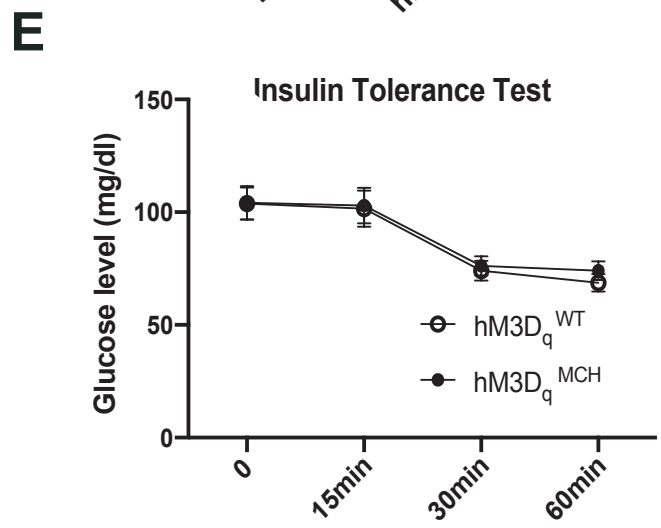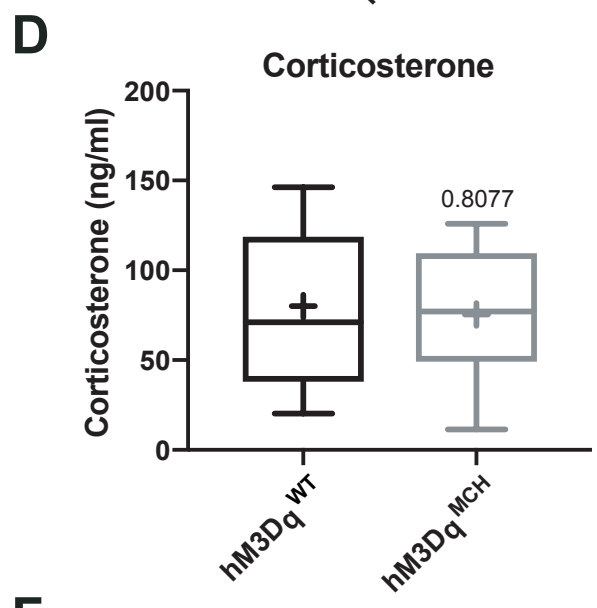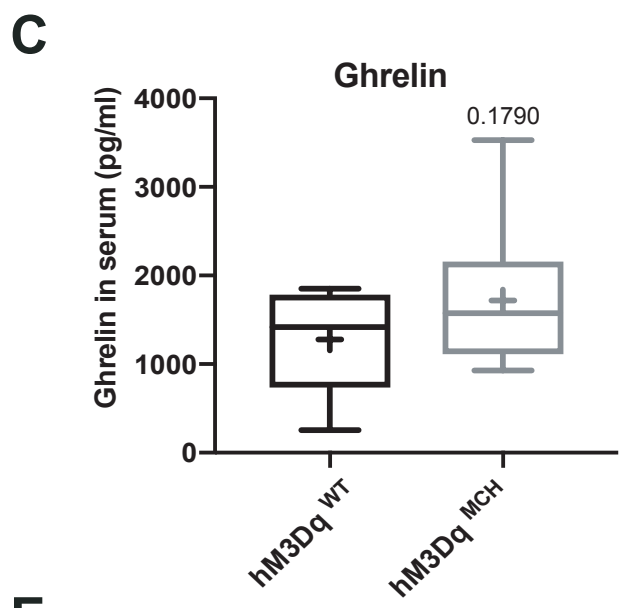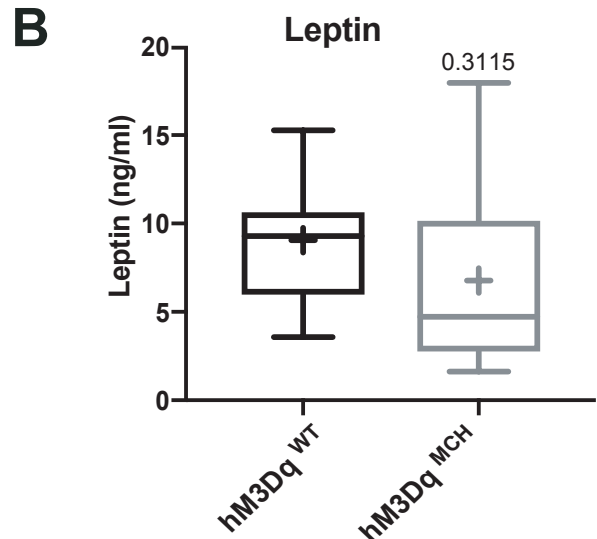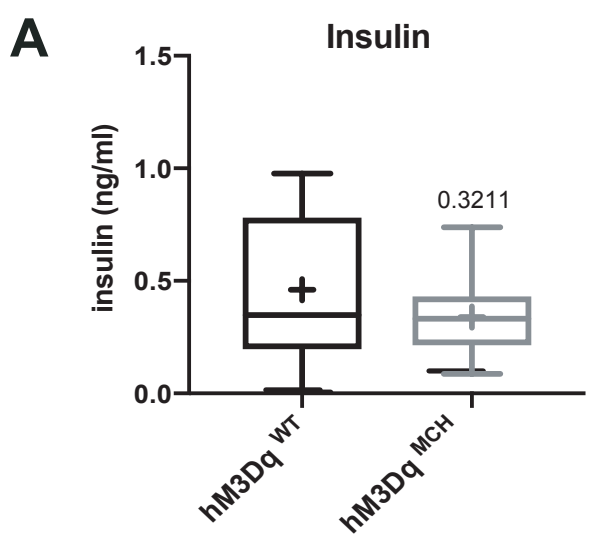
Figure S3. Related to Figure 2 and 3. Systemic metabolic parameters in CNO-treated control and hM3Dq[MCH] mice. (A)-(D) Serum Insulin, Leptin, Ghrelin and Corticosterone levels of fasted and 4 hrs CNO-treated control (n=8-10) and hM3Dq[MCH] mice (n=10-13). (E) and (F) Insulin tolerance test and Glucose tolerance test in fasted and 4 hrs CNO-treated control (n=10) and hM3Dq[MCH] mice (n=13). Statistics: unpaired student T-test,for A-D; Two way ANOVA Sidack Post hoc test, for E and F.

A — 1 hour-Saline

B — 4 hour-Saline

C — 4 hour leptin sensitivity
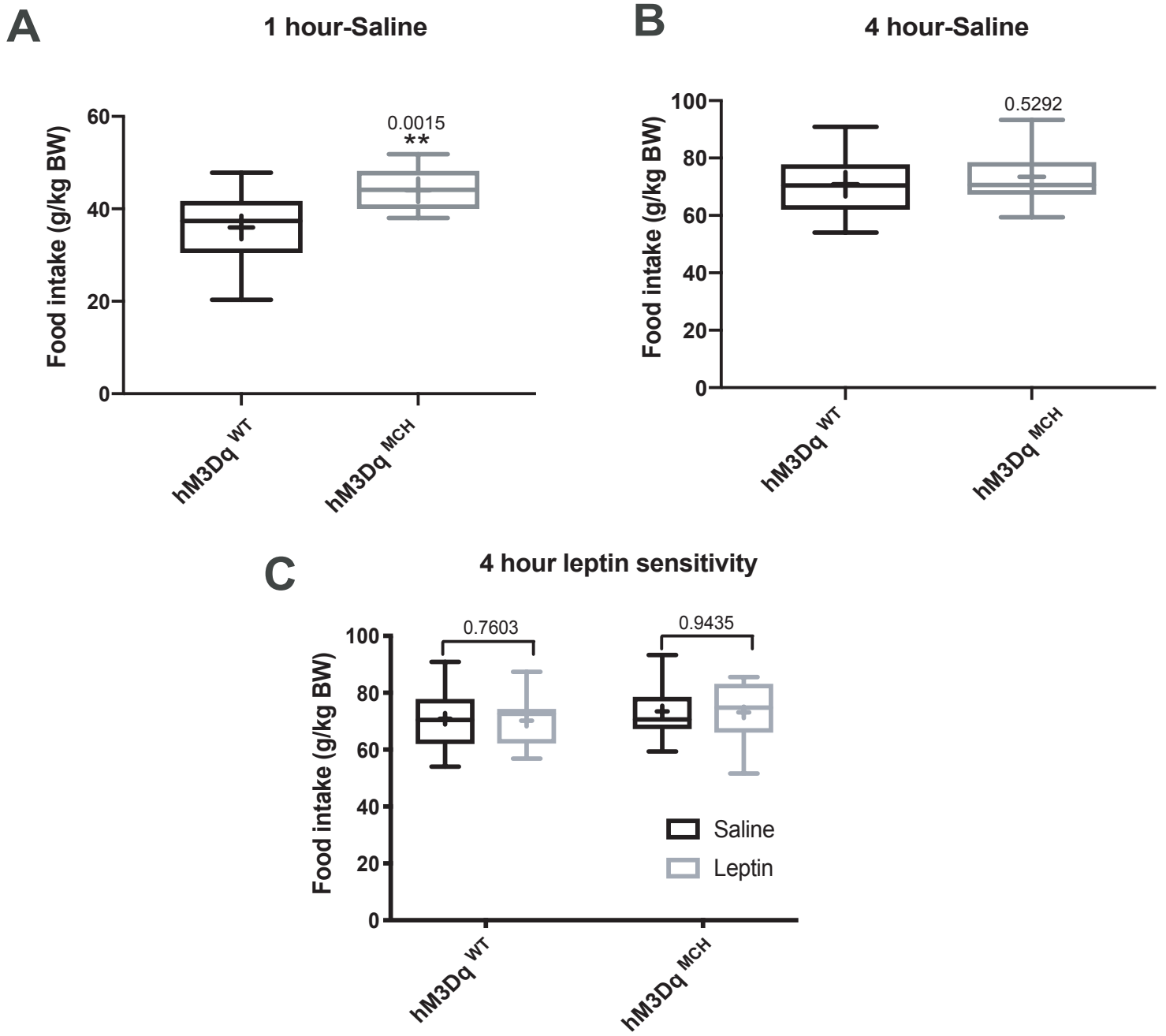
Figure S4. Related to Figure 4. Feeding regulation in hM3Dq^{MCH} mice .
(A) and (B), 1 hr and 4 hrs food intake in fasted and 4 hrs CNO-treated control (n=13) and hM3Dq^{MCH} mice (n=13) with saline (leptin vehicle) injected at half hour before refeeding. (C), Leptin sensitivity at 4 hrs refeeding in fasted and 4 hrs CNO-treated control and hM3Dq^{MCH} mice. Statistics: unpaired Student's T-test, $**p < 0.01$, except paired Student's T-test in leptin sensitivity.

A Fiber placement

B 1 hour-Saline

0.7423

Food intake (g/kg BW)

ChR2 WT   ChR2 MCH

C Fiber placement

hM3Dq WT or MCH mice

D

0.0469
*

Food intake (g/kg BW)

hM3Dq WT   hM3Dq MCH

E 4 hour-Saline

0.9982

Food intake (g/kg BW)

ChR2 WT   ChR2 MCH

F 4 hour leptin sensitivity

Saline
Leptin

0.3983   0.6333

Food intake (g/kg BW)

ChR2 WT   ChR2 MCH
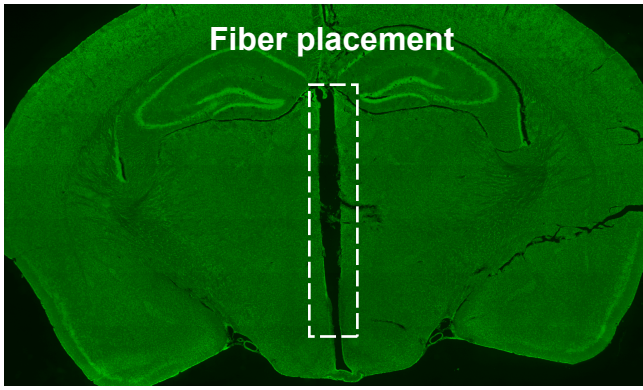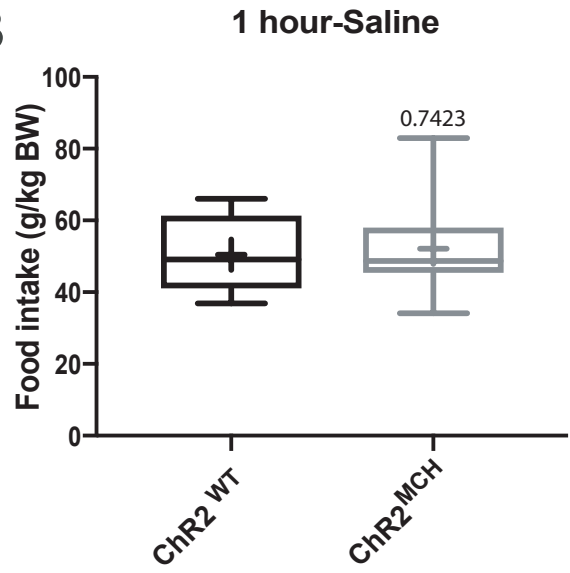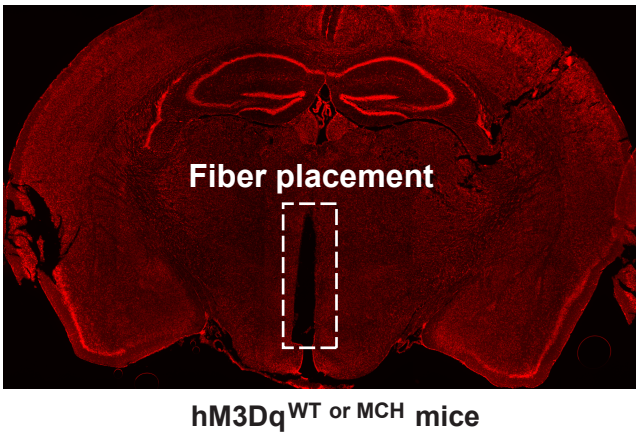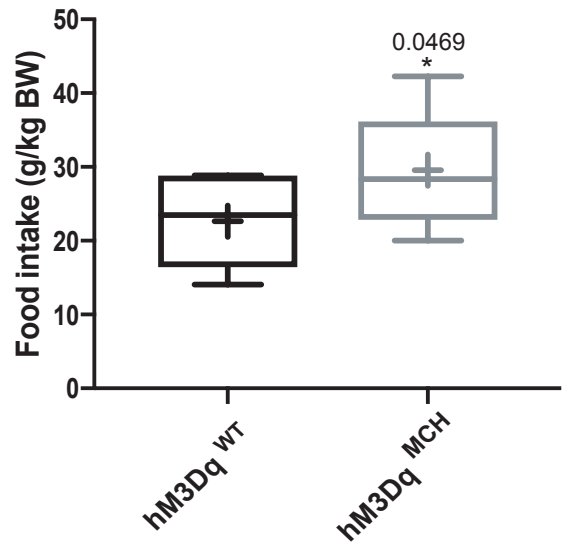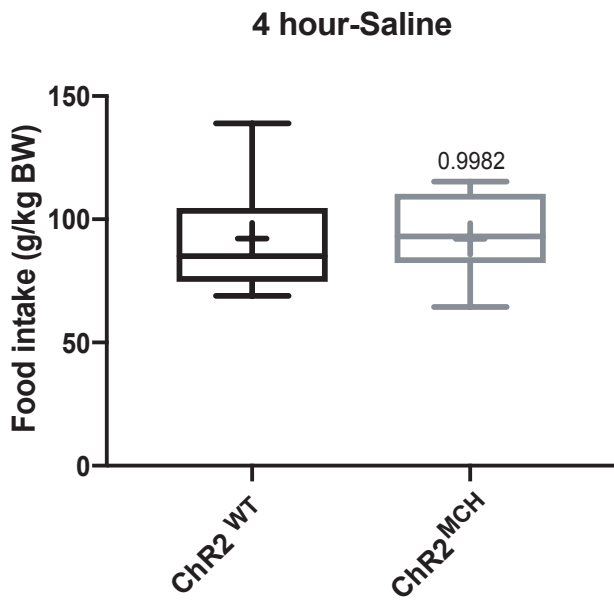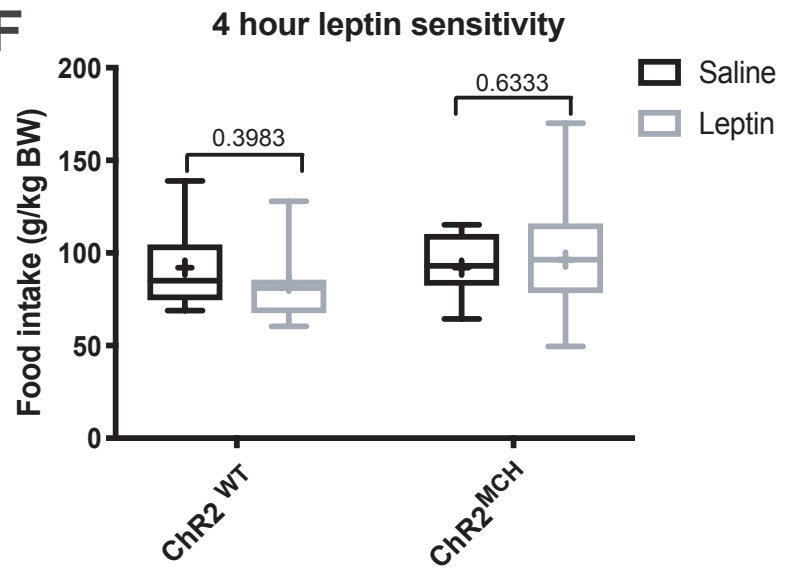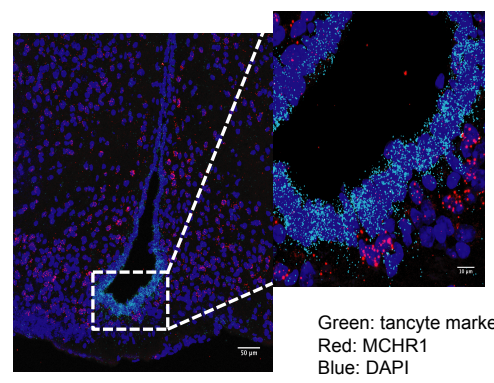
Figure S5. Related to Figure 5. Optogenetic MCH-ME projection stimulation does not change refeeding upon the saline injection. (A) Placement of optical fiber implantation into third ventricle in optogenetic experiments. Green: neuronal tracer stained section from perfused mice with optical fiber implanted. Dashed white square illustrates the fiber trace. (B) 1 hr refeeding in fasted and 3.5 hrs light illuminated control (n=12) and ChR2^{MCH} mice (n=11) injected with saline (leptin vehicle) half hour before refeeding. (C) Placement of optical fiber into control and hM3Dq^{MCH} mice. Red: neuronal tracer stained section from perfused mice with optical fiber implanted. (D) 1 hr food intake in fasted and 4 hrs CNO-treated and fiber implanted control (n=6) and hM3Dq^{MCH} mice (n=8). (E) and (F) 4 hr refeeding in fasted and 3.5 hrs light illuminated control (n=12) and ChR2^{MCH} mice (n=11) injected with saline (leptin vehicle) half hour before refeeding and 4 hrs leptin sensitivity in those mice. Statistics: unpaired Student's T-test, *$p < 0.05$, except paired Student's T-test in leptin sensitivity.

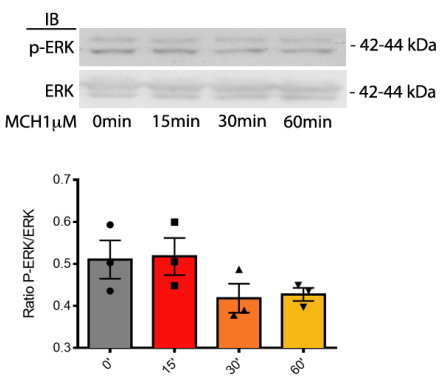**A** qPCR quantification of Mchr1 expression from sorted tancytes

FACS

3V

ARH
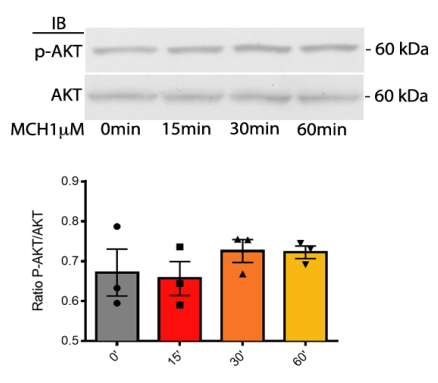tat-cre
ME
tdTomato

Microdissection

Cell dissociation

Pos   Neg

Relative mRNA expression

Negative cells   Tancytes
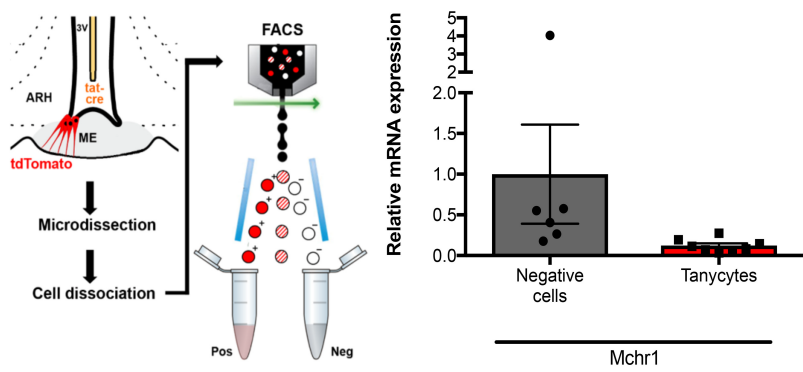
Mchr1

B MCHR1 mRNA *in situ*

Green: tancyte marker
Red: MCHR1
Blue: DAPI
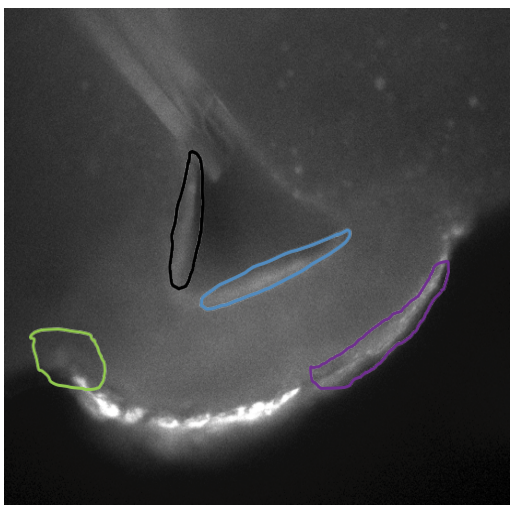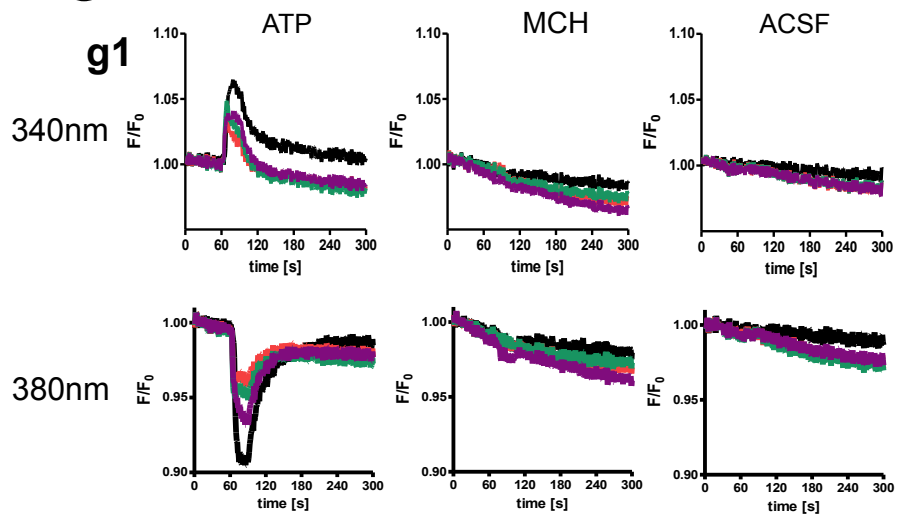
C
IB
p-ERK — 42-44 kDa
ERK — 42-44 kDa
MCH1μM   0min   15min   30min   60min

Ratio P-ERK/ERK
0'   15'   30'   60'

D
IB
p-AKT — 60 kDa
AKT — 60 kDa
MCH1μM   0min   15min   30min   60min

Ratio P-AKT/AKT
0'   15'   30'   60'

E
cAMP concentration (nM)

MCH 1μM without Forskolin
MCH 1μM with Forskolin

MCH Treatment time (min)

F

G

g1   ATP   MCH   ACSF

340nm   F/F$_0$ time [s]

380nm   F/F$_0$ time [s]

g2   α-tanycytes   β-tanycytes

ΔF/F$_0$ time [s]

vessels of the pars tuberalis   blood vessels below the ME

ΔF/F$_0$ time [s]

H

h1   F/F$_0$ time (s)

h2   F/F$_0$ time (s)

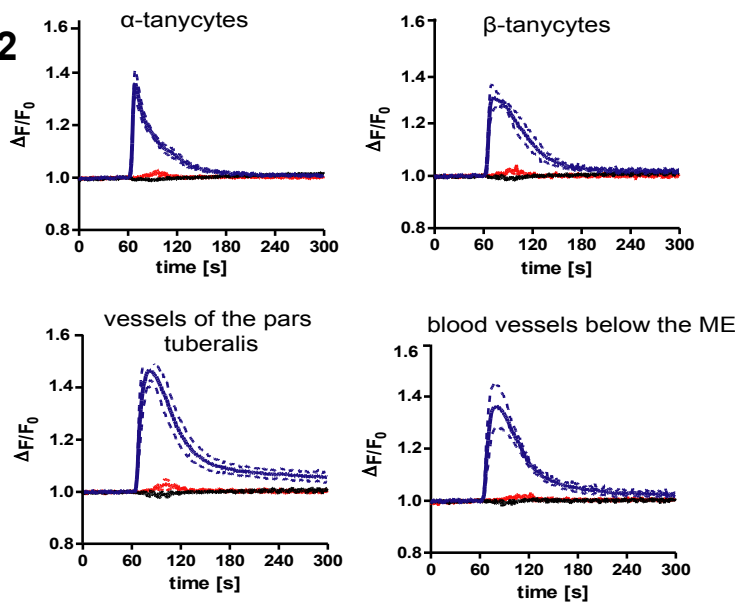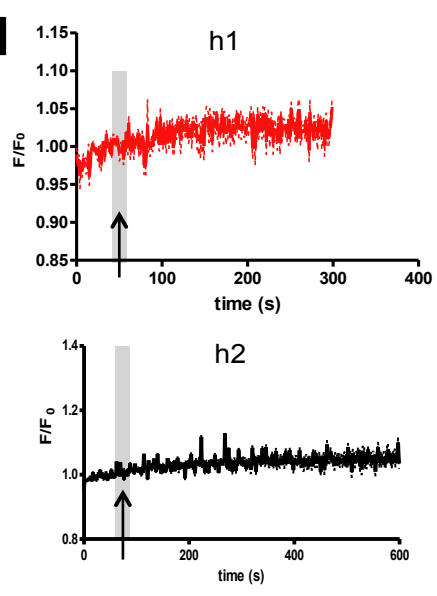**Figure S6. Related to Figure 6 and 7.** MCH does not alter tanycyte signaling.

(A) Illustration of FACS sorted purified tanycytes from the ME (left) and qPCR quantification of Mchr1 expression in purified tdTomato marked tanycytes and non-tdTomato cells of the ME (right). (B) mRNA expression of Mchr1 mRNA by *in situ* hybridization on ME sections. Red, Mchr1; Green, tanycyte marker, Ppp1r1b; Blue, DAPI. (C) Western blotting of ERK and pERK expression after 0, 15 min, 30 min and 60 min of 1 μM MCH incubation (upper panel) and ratio of pERK/ERK expression (lower panel). (D) Western blotting of AKT and pAKT protein expression after 0, 15 min, 30 min and 60 min of 1 μM MCH incubation (upper panel) and ratio of pAKT/AKT comparison (lower panel). (E) cAMP concentration changes after 1 μM MCH 0, 15 min, 30 min and 60 min of incubation with and without forskolin.

(F) Illustration of the regions of interest for calcium imaging in ME slices. (G) Representative time course of fluorescence changes in a living brain slice loaded with Fura2 emitted with 340 nm (g1 upper panel) and 380 nm (g1 lower panel) after direct stimulation with ATP (1 mM, 2 μl over 30 s; a and b), MCH (1 mM, 2 μl over 30 s; c and d) and ACSF (2 μl over 30 s; e and f). Black, alpha tanycytes; red, beta tanycytes; green, blood vessels in the pars tuberalis; purple, blood vessels beneath the median eminence. g2, Average time curves of ΔF/F0 in α-tanycytes, β-tanycytes, vessels of the pars tuberalis and blood vessels beneath the median eminence of 3 brain slices loaded with Fura2 after direct stimulation with ATP (1 mM, 2 μl over 30 s; blue), MCH (1 mM, 2 μl over 30 s; red) and ACSF (2 μl over 30 s; black).

(H) Average of ΔF/F0 in ME-tanycytes of 3 brain slices loaded with Fura2 after direct stimulation with Glutamate (100 μM, 100 μl over 30 s; red) (h1) and baclofen (1 mM, 100 μl over 30 s; black) (h2).
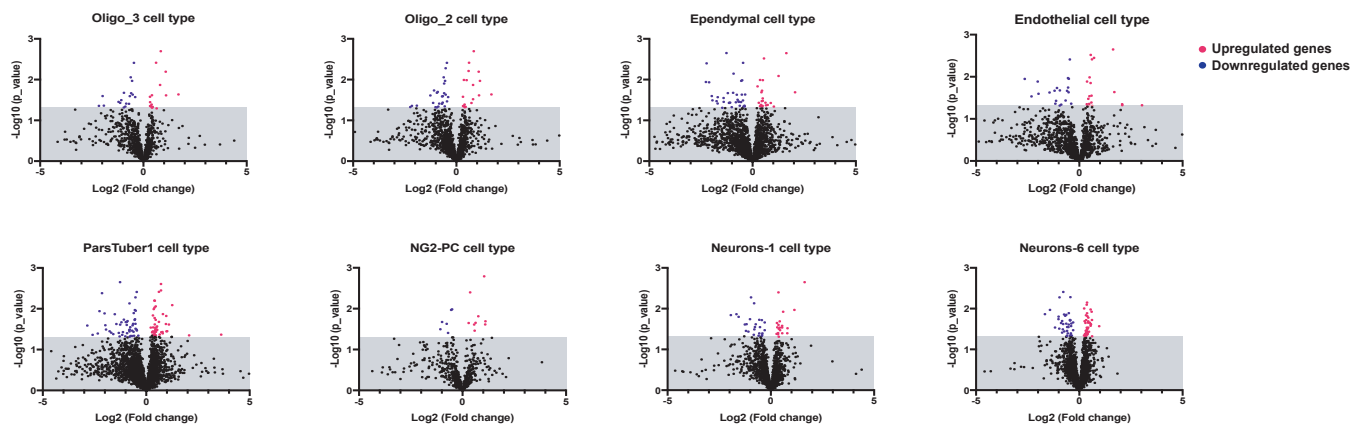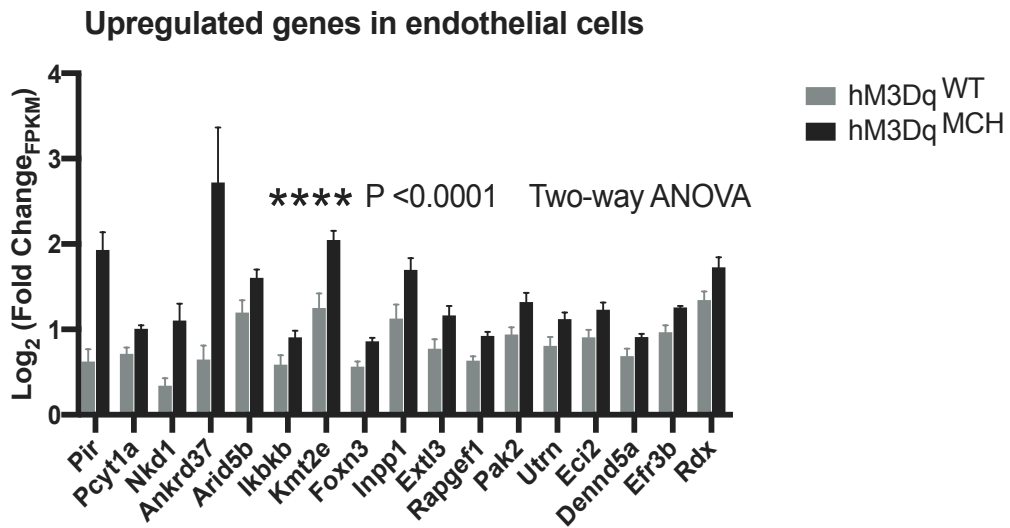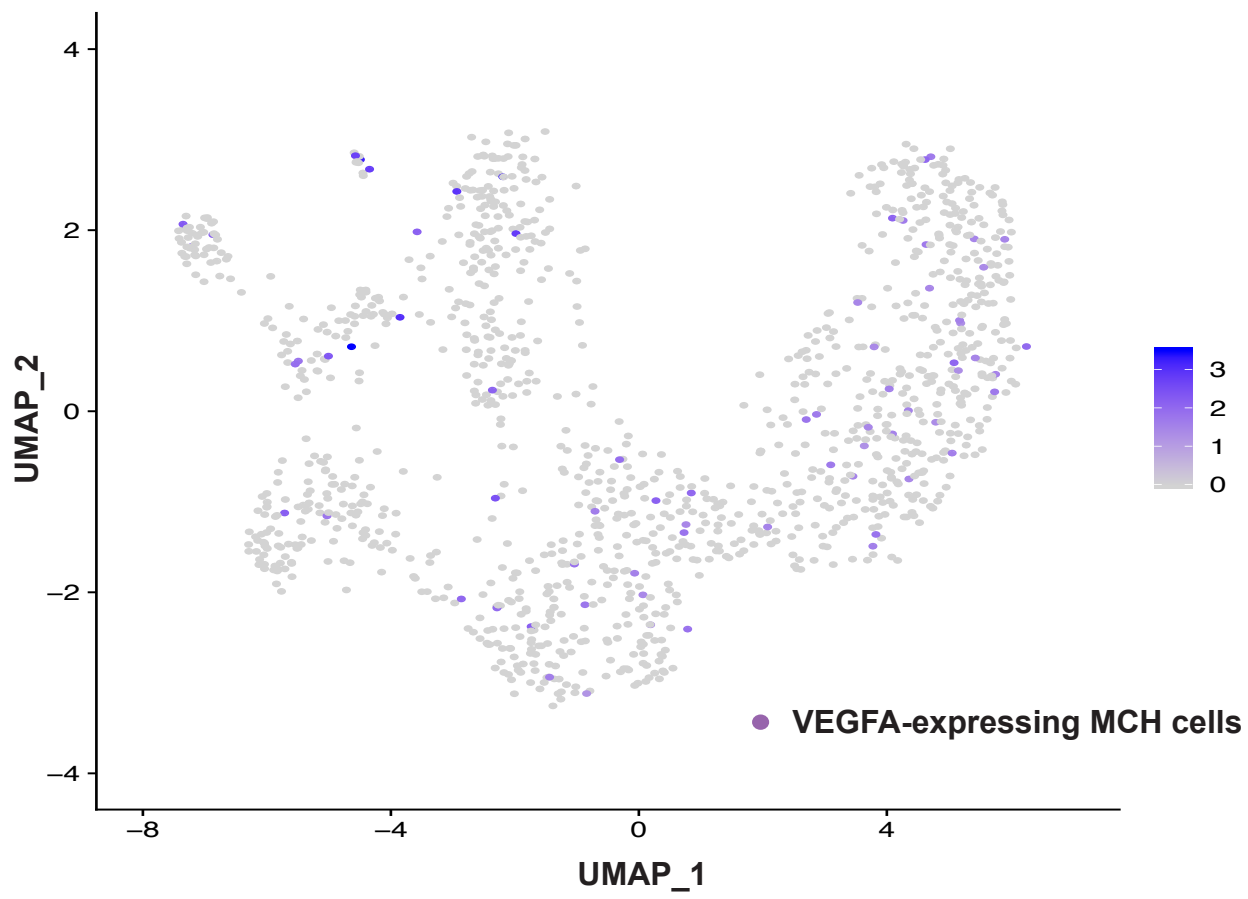
A

Oligo_3 cell type | Oligo_2 cell type | Ependymal cell type | Endothelial cell type

● Upregulated genes
● Downregulated genes

ParsTuber1 cell type | NG2-PC cell type | Neurons-1 cell type | Neurons-6 cell type

(Axes for each plot: x-axis "Log2 (Fold change)", y-axis "-Log10 (p_value)")

B

Upregulated genes in endothelial cells

■ hM3Dq WT
■ hM3Dq MCH

**** P <0.0001   Two-way ANOVA

y-axis: $\text{Log}_2 (\text{Fold Change}_{FPKM})$

Genes: Pir, Pcyt1a, Nkd1, Ankrd37, Arid5b, Ikbkb, Kmt2e, Foxn3, Inpp1, Extl3, Rapgef1, Pak2, Utrn, Eci2, Dennd5a, Efr3b, Rdx

C

Axes: UMAP_2 (y), UMAP_1 (x)

● VEGFA-expressing MCH cells

Figure S7. Related to Figure 6. PhosphoRibotrap-based analysis of all cell types regulated by MCH neuron activation.
(A) Neuronal, glia and endothelial cell types in the ARC were regulated in 1 hr CNO treated hM3Dq^{MCH} mice.
(B) Enriched gene expression of endothelial cell cluster in control and hM3Dq^{MCH} mice. (C) VEGFA expressing cells are distributed cross all the clusters of MCH neurons. Purple dots represent VEGFA positive cells.